

## REVISED STELLAR PROPERTIES OF KEPLER TARGETS FOR THE QUARTER 1–16 TRANSIT DETECTION RUN

DANIEL HUBER<sup>1,2</sup>, VICTOR SILVA AGUIRRE<sup>3</sup>, JAYMIE M. MATTHEWS<sup>4</sup>, MARC H. PINSONNEAULT<sup>5</sup>, ERIC GAIDOS<sup>6</sup>, RAFAEL A. GARCÍA<sup>7</sup>, SASKIA HEKKER<sup>8,9</sup>, SAVITA MATHUR<sup>10</sup>, BENOÎT MOSSER<sup>11</sup>, GUILLERMO TORRES<sup>12</sup>, FABIENNE A. BASTIEN<sup>13</sup>, SARBANI BASU<sup>14</sup>, TIMOTHY R. BEDDING<sup>15,3</sup>, WILLIAM J. CHAPLIN<sup>16,3</sup>, BRICE-OLIVIER DEMORY<sup>17</sup>, SCOTT W. FLEMING<sup>18</sup>, ZHAO GUO<sup>19</sup>, ANDREW W. MANN<sup>20</sup>, JASON F. ROWE<sup>1,2</sup>, ALDO M. SERENELLI<sup>21</sup>, MYRON A. SMITH<sup>22</sup>, AND DENNIS STELLO<sup>15,3</sup>

*accepted for publication in ApJS*

### ABSTRACT

We present revised properties for 196,468 stars observed by the NASA Kepler Mission and used in the analysis of Quarter 1–16 (Q1–Q16) data to detect and characterize transiting planets. The catalog is based on a compilation of literature values for atmospheric properties (temperature, surface gravity, and metallicity) derived from different observational techniques (photometry, spectroscopy, asteroseismology, and exoplanet transits), which were then homogeneously fitted to a grid of Dartmouth stellar isochrones. We use broadband photometry and asteroseismology to characterize 11,532 *Kepler* targets which were previously unclassified in the Kepler Input Catalog (KIC). We report the detection of oscillations in 2,762 of these targets, classifying them as giant stars and increasing the number of known oscillating giant stars observed by *Kepler* by  $\sim 20\%$  to a total of  $\sim 15,500$  stars. Typical uncertainties in derived radii and masses are  $\sim 40\%$  and  $\sim 20\%$ , respectively, for stars with photometric constraints only, and 5 – 15% and  $\sim 10\%$  for stars based on spectroscopy and/or asteroseismology, although these uncertainties vary strongly with spectral type and luminosity class. A comparison with the Q1–Q12 catalog shows a systematic decrease in the radii of M dwarfs, while radii for K dwarfs decrease or increase depending on the Q1–Q12 provenance (KIC or Yonsei-Yale isochrones). Radii of F–G dwarfs are on average unchanged, with the exception of newly identified giants. The Q1–Q16 star properties catalog is a first step towards an improved characterization of all *Kepler* targets to support planet occurrence studies.

*Subject headings:* stars: fundamental parameters — stars: oscillations — techniques: photometric — catalogs — planetary systems

### 1. INTRODUCTION

The unprecedented precision of photometric data collected by the NASA *Kepler* mission (Borucki et al. 2010; Koch et al. 2010b) has revolutionized planetary and stellar astrophysics over the past years. Examples of breakthrough discoveries in exoplanet science include more than 2700 new planet candidates (Borucki et al. 2011a,b; Batalha et al. 2013; Burke et al. 2014), measurements of planet densities in multi-planet systems through transit timing variations (Holman et al. 2010; Lissauer et al. 2011; Carter et al. 2012), the detection of small planets in or near the habitable zone (Borucki et al. 2012, 2013; Barclay et al. 2013b), and the discovery of single and multi-planet systems around binary stars (Doyle et al. 2011; Welsh et al. 2012; Orosz et al. 2012a). At the same time, *Kepler* data allowed key advances in stellar astrophysics such as the detection of more than 2000 eclipsing binary stars (Prša et al. 2011; Slawson et al.

ogy, 77 Massachusetts Ave., Cambridge, MA 02139, USA

<sup>18</sup> Space Telescope Science Institute, 3700 San Martin Drive, Baltimore, Maryland 21218, USA

<sup>19</sup> Center for High Angular Resolution Astronomy, Georgia State University, PO Box 3969, Atlanta, GA 30302, USA

<sup>20</sup> Institute for Astronomy, University of Hawaii, 2680 Woodlawn Drive, Honolulu, HI 96822, USA

<sup>21</sup> Instituto de Ciencias del Espacio (CSIC-IEEC), Facultad de Ciencias, 08193 Bellaterra, Spain

<sup>22</sup> NOAO, 950 N. Cherry Ave., Tucson, AZ 85719, USA

<sup>1</sup> NASA Ames Research Center, Moffett Field, CA 94035, USA; daniel.huber@nasa.gov

<sup>2</sup> SETI Institute, 189 Bernardo Avenue, Mountain View, CA 94043, USA

<sup>3</sup> Stellar Astrophysics Centre, Department of Physics and Astronomy, Aarhus University, Ny Munkegade 120, DK-8000 Aarhus C, Denmark

<sup>4</sup> Department of Physics and Astronomy, University of British Columbia, Vancouver, Canada

<sup>5</sup> Department of Astronomy, Ohio State University, OH 43210, USA

<sup>6</sup> Department of Geology and Geophysics, University of Hawaii at Manoa, Honolulu, HI 96822, USA

<sup>7</sup> Laboratoire AIM, CEA/DSM-CNRS, Université Paris 7 Diderot, IRFU/SAP, Centre de Saclay, 91191, Gif-sur-Yvette, France

<sup>8</sup> Max-Planck-Institut für Sonnensystemforschung, Justus-von-Liebig-Weg 3, 37077 Göttingen, Germany

<sup>9</sup> Astronomical Institute 'Anton Pannekoek', University of Amsterdam, Science Park 904, 1098 XH Amsterdam, The Netherlands

<sup>10</sup> Space Science Institute, 4750 Walnut Street Suite 205, Boulder, CO 80301, USA

<sup>11</sup> LESIA, CNRS, Université Pierre et Marie Curie, Université Denis. Diderot, Observatoire de Paris, 92195 Meudon cedex, France

<sup>12</sup> Harvard-Smithsonian Center for Astrophysics, Cambridge, Massachusetts 02138, USA

<sup>13</sup> Department of Physics & Astronomy, Vanderbilt University, 1807 Station B, Nashville, TN 37235, USA

<sup>14</sup> Department of Astronomy, Yale University, New Haven, CT 06511, USA

<sup>15</sup> Sydney Institute for Astronomy (SIfA), School of Physics, University of Sydney, NSW 2006, Australia

<sup>16</sup> School of Physics and Astronomy, University of Birmingham, Birmingham B15 2TT, UK

<sup>17</sup> Department of Physics, Massachusetts Institute of Technol-

2011; Matijević et al. 2012) including eclipsing triple systems (Carter et al. 2011; Derekas et al. 2011), the study of the core structure and rotation of subgiant and red-giant stars (Bedding et al. 2011; Beck et al. 2011; Mosser et al. 2012b; Deheuvelds et al. 2012), an order of magnitude increase of known dwarf stars with detected oscillations (Chaplin et al. 2011), and the discovery of tidal pulsations in eccentric binary systems (Thompson et al. 2012).

In addition to characterizing individual exoplanet systems, a primary mission goal of *Kepler* is to determine the frequency of Earth-sized planets in the habitable zones of Sun-like stars. Planet occurrence rates crucially depend not only on our knowledge of properties such as radii and luminosities of the host stars (which in turn determine the properties of the planets), but also on our understanding of the properties of the *parent sample*. For example, if a significant number of subgiant or giant stars have been misclassified as dwarfs, this would bias occurrence rates since small planets are harder to detect around larger stars.

Many studies which have explored planet-occurrence rates using the *Kepler* sample (e.g., Catanzarite & Shao 2011; Howard et al. 2012; Traub 2012; Dong & Zhu 2013; Fressin et al. 2013; Petigura et al. 2013a,b) have mostly relied on stellar properties based on the Kepler Input Catalog (KIC, Brown et al. 2011, hereafter B11). The primary purpose of the KIC was to discern dwarfs from giants to optimize the target selection towards finding Earth-sized planets in the habitable zones of Sun-like stars (Batalha et al. 2010). As emphasized by B11, the methodology behind constructing the KIC limits its use beyond target selection. Recent planet-occurrence studies have used improved stellar properties either for specific parameter ranges such as cool dwarfs (Dressing & Charbonneau 2013; Morton & Swift 2013), or for a wide range of spectral types for dwarfs (Gaidos 2013). However, a revised characterization of the full target sample to support the *Kepler* planet-detection pipeline and planet-occurrence studies has yet to be completed.

Since the creation of the KIC, a large number of new observations have become available. For example, new broadband photometry covering the full *Kepler* field has been completed (Everett et al. 2012; Greiss et al. 2012). Additionally, a large amount of spectroscopic follow-up observations have been performed within the Kepler Community Follow-Up Program (CFOP<sup>23</sup>), and systematic spectroscopic surveys of the *Kepler* field using multi-object fiber-fed spectrographs are currently in progress (Zasowski et al. 2013; Pinsonneault et al. 2014). Importantly, *Kepler* light curves themselves contain information about fundamental properties of stars. In particular, *Kepler* has allowed the application of asteroseismology to stars ranging from hot, compact objects (Kawaler et al. 2010; Østensen et al. 2011), to classical pulsators (Grigahcène et al. 2010; Kolenberg et al. 2010; Kurtz et al. 2011), cool dwarfs (Chaplin et al. 2011; Silva Aguirre et al. 2011; Mathur et al. 2012) and red giant stars (Bedding et al. 2010; Hekker et al. 2011; Kallinger et al. 2010; Mosser et al. 2012a).

Many of these results have not yet been taken into

account in planet occurrence studies due to the lack of catalogs covering most *Kepler* targets. In this paper we present a catalog of revised properties for 196,468 *Kepler* targets based on a consolidation of literature values and the first characterization of unclassified stars in the KIC.

## 2. KEPLER INPUT CATALOG

We begin with a brief review of the Kepler Input Catalog. As described by B11, the primary observables for the KIC stellar classification pipeline (SCP) were KIC *griz* and 2MASS *JHK* broadband photometry (Skrutskie et al. 2006), supplemented by an intermediate-band *D51* filter (centered on the Mg Ib lines at 510 nm). These data were used to calculate seven independent colors, which were then compared to synthetic colors calculated from ATLAS9 model atmospheres (Castelli & Kurucz 2004). To account for interstellar extinction, B11 adopted a simple reddening model giving 1 magnitude of *V*-band extinction per 1 kpc in the galactic plane, decreasing with galactic latitude with an *e*-folding scale height of 150 pc. To overcome degeneracies of matching broadband colors to models to estimate effective temperature ( $T_{\text{eff}}$ ), surface gravity ( $\log g$ ) and metallicity ( $[\text{Fe}/\text{H}]$ ), three priors were adopted: a metallicity prior based on a solar-neighborhood distribution of the Geneva-Copenhagen survey (Nordström et al. 2004), a  $T_{\text{eff}}\text{-}\log g$  prior based on the number density of stars in the Hipparcos catalog (van Leeuwen 2007), and a prior on the number density of stars as a function of galactic latitude. Stellar masses and luminosities were derived from average relations between  $T_{\text{eff}}$ ,  $\log g$ , luminosity and mass calculated from Padova isochrones (Girardi et al. 2000). Finally, stellar radii were calculated from the derived effective temperatures and luminosities.

The difficulty of estimating stellar properties (in particular  $\log g$  and  $[\text{Fe}/\text{H}]$ ) from broadband colors resulted in a number of shortcomings which limited the use of the KIC beyond target selection. Follow-up studies have since tested stellar properties in the KIC to quantify these shortcomings. The main conclusions of these tests can be summarized as follows:

- KIC surface gravities are frequently overestimated by up to 0.2 dex, resulting in underestimated radii by up to 50% (Verner et al. 2011; Everett et al. 2013). Observational biases also suggest that the fraction of subgiant stars in the *Kepler* target sample may be underestimated (Gaidos & Mann 2013).
- KIC temperatures are on average 200 K cooler than temperatures based on the Sloan system or the infrared flux method (Pinsonneault et al. 2012, hereafter P12). KIC *griz* photometry also shows a color-dependent offset to Sloan DR9 photometry.
- A large fraction of bright ( $Kp < 14$ ) late-K to mid-M type stars are misclassified as dwarfs (Mann et al. 2012). Furthermore, surface gravities, metallicities and radii for genuine late-type dwarfs are systematically biased (Muirhead et al. 2012a; Batalha et al. 2013; Dressing & Charbonneau 2013).
- Roughly 5% of Kepler targets have KIC parameters that should be absent in a well-studied field population, specifically G-type dwarfs with  $\log g \sim 5$

<sup>23</sup> <https://cfop.ipac.caltech.edu/home/login.php>

and K-dwarfs with  $T_{\text{eff}} \sim 5000\text{K}$  and  $\log g \sim 4.2$  (Batalha et al. 2013). We refer to these stars in the following as “No-Man’s-Land” stars.

Similar conclusions have been found theoretically by Farmer et al. (2013), who processed a synthetic stellar population of the *Kepler* field through the KIC classification pipeline. We note that most of the above shortcomings have already been anticipated and emphasized by B11.

### 3. STELLAR MODELS

In general, determining stellar masses and radii involves a comparison of observations with models. For the current catalog, we adopted the 2012 isochrones from the Dartmouth Stellar Evolution Database (DSEP, Dotter et al. 2008)<sup>24</sup>. We have used the DSEP interpolation routine to produce a grid of 1 – 15 Gyr isochrones in steps of 0.5 Gyr in age and 0.02 dex in  $[\text{Fe}/\text{H}]$ . Only models with solar-scaled alpha-element abundances have been included. In addition to low-mass models, we supplemented the grid with 0.25 – 1 Gyr isochrones with the default metallicity spacing ( $-2.5$ ,  $-2.0$ ,  $-1.5$ ,  $-1.0$ ,  $-0.5$ ,  $0.07$ ,  $0.15$ ,  $0.36$  and  $0.5$  dex). The full grid includes approximately  $1.5 \times 10^6$  individual models.

The choice of DSEP was motivated by the good agreement with models by Baraffe et al. (1998), which have been demonstrated to reasonably reproduce observations of low-mass dwarfs with empirically measured radii, masses and effective temperatures from long-baseline interferometry (Boyajian et al. 2012, 2013) or low-mass eclipsing binary systems (Kraus et al. 2011; Carter et al. 2011) (although significant offsets still exist, see Boyajian et al. 2013). Additionally, DSEP models cover a large parameter space and include broadband colors based on PHOENIX model atmospheres (Hauschildt et al. 1999) for most filters with available data for *Kepler* targets. We note that the adopted isochrone grid does not include He-core burning models for stars which undergo the helium flash ( $M \lesssim 2 M_{\odot}$ ). As emphasized in Section 8, this introduces a significant bias for derived masses and radii of giant stars in the catalog.

The coolest DSEP models for dwarfs have temperatures close to 3200 K. However, recent spectroscopic follow-up observations revealed a significant number of ultra-cool dwarfs in the Kepler field (Martín et al. 2013), and additional late-type M dwarfs have been added to the *Kepler* target list through Guest Observer programs<sup>25</sup>. To characterize these stars, we fit second to fourth order polynomials between colors, temperatures, gravities, and radii to  $> 2$  Gyr BT-Settl isochrones (Allard et al. 2012) with temperatures between 2000 – 3400 K. These polynomials were then used to interpolate the BT-Settl grid and provide typical stellar properties for a given color or temperature.

### 4. CONSOLIDATION OF LITERATURE VALUES

We have collected published values for  $T_{\text{eff}}$ ,  $\log g$  and  $[\text{Fe}/\text{H}]$  for all *Kepler* targets. We only considered publications that have derived stellar properties for more than

one star, with the exception of confirmed exoplanet host stars. We considered five main data sources:

- **Asteroseismology:** Stellar oscillations provide accurate measurements of stellar properties such as density and surface gravity (Stello et al. 2008; Bedding 2011; Miglio et al. 2012; Huber et al. 2012; Silva Aguirre et al. 2012; Hekker et al. 2013). For cool stars with asteroseismic detections but without published  $\log g$  values, we have used the observed frequency of maximum power ( $\nu_{\text{max}}$ ) to estimate  $\log g$  through the scaling relation  $\nu_{\text{max}} \propto g T_{\text{eff}}^{-0.5}$  (Brown et al. 1991; Belkacem et al. 2011), where  $T_{\text{eff}}$  was adopted either from photometry or spectroscopy, as described below.
- **Transits:** Transiting exoplanets allow accurate measurements of the mean stellar density if the orbital eccentricity and impact parameter are accurately known (see, e.g., Seager & Mallén-Ornelas 2003; Brown 2010; Winn 2010). For multi-planet systems in particular, transit-derived stellar densities reach uncertainties comparable to asteroseismology and are often preferred over constraints on  $\log g$  from spectroscopy (Lissauer et al. 2013; Jontof-Hutter et al. 2013). This category also includes host stars in eclipsing double-lined spectroscopic binaries with dynamically measured masses and radii, which can be combined to calculate  $\log g$ .
- **Spectroscopy:** Modeling spectra is one of the most traditional methods to derive  $T_{\text{eff}}$ ,  $\log g$  and  $[\text{Fe}/\text{H}]$ , although some limitations of spectroscopic surface gravities exist (Torres et al. 2012; Huber et al. 2013a). We have only adopted published solutions based on high-resolution ( $R \gtrsim 20000$ ) spectra. We note that the properties are based on different spectroscopic analysis pipelines such as SME (Spectroscopy Made Easy, Valenti & Piskunov 1996), SPC (Stellar Parameter Classification, Buchhave et al. 2012), VWA (Versatile Wavelength Analysis, Bruntt et al. 2010), and ROTFIT (Frasca et al. 2003), and hence are not homogeneous.
- **Photometry:** Broadband photometry is a well established method to determine temperatures (e.g., Casagrande et al. 2010), with narrow-band filters allowing some sensitivity to  $\log g$  and  $[\text{Fe}/\text{H}]$ . This category includes literature using revised KIC photometry, in particular the temperature scale revision by P12.
- **KIC:** For this category, original Kepler Input Catalog values have been adopted. Note that this category is listed separately from photometry to discern it from literature values published after the launch of the *Kepler* mission.

Table 1 lists the adopted prioritization scheme for stars with literature values from more than one source, and Figure 1 shows the main categories in a  $\log g$  versus  $T_{\text{eff}}$  diagram.

<sup>24</sup> <http://stellar.dartmouth.edu/models/index.html>

<sup>25</sup> <http://keplerscience.arc.nasa.gov/>

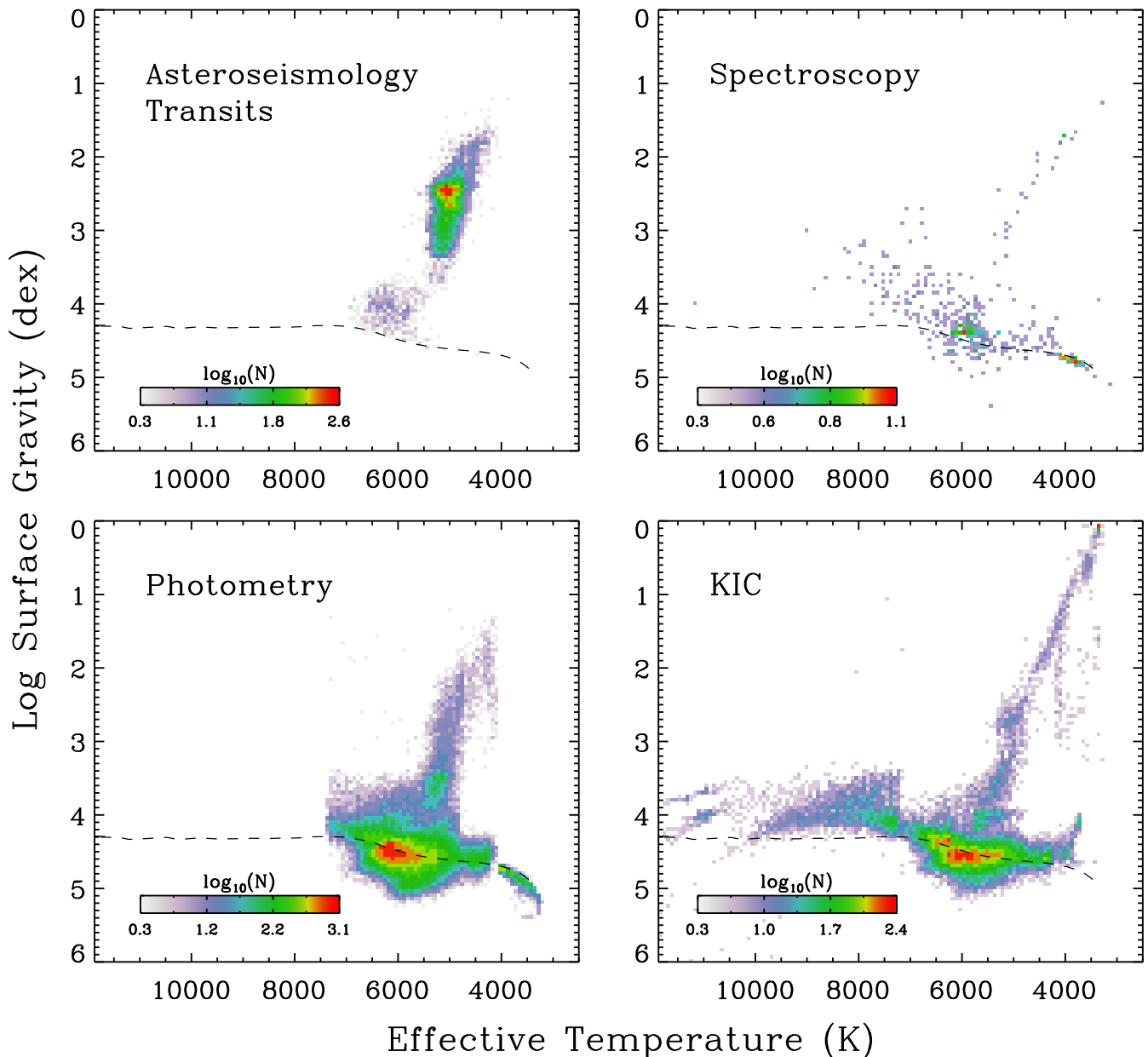


FIG. 1.— Surface gravity versus effective temperature for the main categories of consolidated literature input for the Q1–Q16 catalog. Colors denote the relative logarithmic number density of stars as given in the legend. The black dashed line shows the solar-metallicity zero-age main sequence for Dartmouth models. Following the notation in Table 1, the panels include the following categories: 1 – 5 (top left), 7 – 10 (top right), 11 – 12 (bottom left) and 13 (bottom right). Note that unclassified stars (categories 6 and 14) are not included in this figure.

Categories 1–2 include the “gold-standard” sample of  $\sim 250$  stars for which both high-resolution spectroscopy and either asteroseismology or transit-derived densities are available. This combination removes degeneracies in the spectroscopic analysis and typically leads to best possible characterization of *Kepler* targets (except for bright stars with measured parallaxes).

Categories 3–6 contain stars with asteroseismic surface gravities for which no spectroscopic effective temperatures or metallicities are available. For most of these stars, temperatures from P12 were adopted. To ensure consistency between the P12 temperatures (which were calibrated to  $[\text{Fe}/\text{H}] = -0.2$ ) and the adopted metallic-

ities (mostly based on KIC values), we have corrected the temperatures using Table 4 in P12<sup>26</sup>. We emphasize that KIC metallicities are valid only in a statistical sense, but are not accurate on a star-by-star basis (Brown et al. 2011; Bruntt et al. 2011; Dong et al. 2013). Category 6 includes giant stars which were so far unclassified in the KIC, but yielded an asteroseismic detection in this study (see Section 5).

<sup>26</sup> Note that due to an error in copying the table, the corrected temperatures are cooler than when using the original P12 corrections. However, the effect is only a few degrees on average and 20 K at maximum, and hence negligible compared to the uncertainties.

TABLE 1  
CATEGORIES OF LITERATURE INPUT

$C$	$T_{\text{eff}}$	$\log g$	[Fe/H]	$N$
1	spectroscopy	asteroseismology	spectroscopy	258
2	spectroscopy	transits	spectroscopy	20
3	spectroscopy	asteroseismology	photometry	7
4	photometry	asteroseismology	photometry	429
5	photometry	asteroseismology	KIC	12488
6	unclassified	asteroseismology	unclassified	2762
7	spectroscopy	spectroscopy	spectroscopy	486
8	spectroscopy	photometry	spectroscopy	32
9	spectroscopy	photometry	photometry	310
10	phot./KIC	phot./KIC	spectroscopy	23
11	photometry	photometry	photometry	3904
12	photometry	KIC	KIC	135278
13	KIC	KIC	KIC	32042
14	unclassified	unclassified	unclassified	8429
All	—	—	—	196468

Note:  $C$  indicates the priority for each category, and  $N$  denotes the number of stars in that category.

Category 7 comprises stars characterized by high-resolution spectroscopy only. This includes large spectroscopic surveys such as Buchhave et al. (2012) for F–K dwarfs, Muirhead et al. (2012a) for M dwarfs, and Uytterhoeven et al. (2011) for A–F stars. Categories 8–10 include stars for which at least one property has been determined through spectroscopy, with the remaining properties constrained by photometry or the KIC.

Category 11 contains stars whose properties are solely based on new broadband photometry. This category is dominated by Dressing & Charbonneau (2013), and the study of planet-candidate hosts by Gaidos (2013).

Category 12 comprises stars with revised temperatures from P12 combined with KIC  $\log g$  and [Fe/H]. The same  $T_{\text{eff}}$  corrections as described for Category 5 have been adopted. We note that this category includes nearly 70% of the full sample.

Category 13 includes stars that only have KIC parameters available. Stars in this category make up roughly 15% of the target sample, and either fell outside the temperature range of the P12 calibration, or were not assigned  $T_{\text{eff}}$  values due to a lack of good 2MASS photometry. To ensure consistency with the remaining sample, KIC temperatures were corrected by interpolating the statistical corrections in Table 8 of P12.

Finally, category 14 comprises stars that were unclassified in the KIC and did not yield an asteroseismic detection in this study. The characterization of unclassified stars is described in detail in the next section.

We note that the literature search was optimized for relatively unevolved stars and hence did not include certain late stages of evolution such as RR Lyrae stars. For more accurate stellar properties of these stars we refer the reader to spectroscopic follow-up studies that have not been considered here (e.g., Nemeč et al. 2013).

## 5. UNCLASSIFIED STARS

Approximately 7% of *Kepler* targets do not have stellar properties listed in the KIC due to the lack of data in one or more filters. As described in Batalha et al. (2010) these targets are bright stars ( $Kp < 14$ ) which were added to supplement the original exoplanet target

list. Approximately one quarter of these stars were consequently dropped from the target list based on a photometric luminosity classification using Q1 observations. In previous runs of the *Kepler* planet detection pipeline (Jenkins et al. 2010b) unclassified stars were assumed to have solar properties, while for planet-candidate catalogs typical main-sequence values based on  $J - K$  colors were used. In the following section we describe a first effort for a comprehensive classification of unclassified *Kepler* targets based on broadband photometry and asteroseismology.

### 5.1. Asteroseismic Analysis and Luminosity Classification

The first step in the classification process was to discern dwarfs from giant stars. As described by Batalha et al. (2010) and Huber et al. (2013a), asteroseismology is an efficient tool to identify giant stars using *Kepler* data since the oscillation amplitudes are large enough to be detectable independent of shot noise, and because oscillation timescales are long enough to be measurable with long-cadence data. We have analyzed Q0–14 long-cadence data of 13420 unclassified stars using the asteroseismic detection pipelines described by Huber et al. (2009), Hekker et al. (2010), Mosser & Appourchaux (2009) and Mathur et al. (2010). We have used simple-aperture photometry (SAP) data as opposed to the Pre-search Data Conditioning (PDC) data (Smith et al. 2012; Stumpe et al. 2012) in order to preserve long-periodic oscillations typical for high-luminosity giant stars. Instrumental trends such as inter-quarter flux discontinuities and pixel-sensitivity dropouts were corrected by fitting linear functions to the start and end of each subset, and by applying a quadratic Savitzky-Golay filter (Savitzky & Golay 1964) with a width of 20 days. In a few stars, we have also applied the procedures described in García et al. (2011) to double check that features in the light curves were not a consequence of the correction procedures and hence verify the reliability of the seismic solutions.

Of the 13420 stars analyzed, 3114 targets showed oscillations that classified them as giants. A subset of 1760 of these targets have been observed for more than 9 quarters between Q1-16, with 1176 targets of this subset having been observed continuously for the entire mission. The new detections presented here raise the number of oscillating giant stars detected by *Kepler* by  $\sim 20\%$  over previous detections (Hekker et al. 2011; Stello et al. 2013) to a total of  $\sim 15500$  stars. Importantly, the newly detected oscillating giants predominantly have surface gravities well below the red clump ( $\log g < 2$ , see Section 5.3). Such stars are underrepresented in previous asteroseismic samples and provide the opportunity to study oscillations in late stages of stellar evolution such as the tip of the red giant branch and the asymptotic giant branch (Bányai et al. 2013; Mosser et al. 2013). Our analysis also yielded 475 classical pulsators, such as  $\gamma$  Doradus and  $\delta$  Scuti stars, which were identified using the automated classification pipeline by Debosscher et al. (2011).

Figure 2 shows 2MASS  $J - H$  versus  $H - K$  diagrams for the unclassified sample considered in this study. Note that we have rejected stars without AAA-quality 2MASS photometry from the catalog, reducing the initial sam-

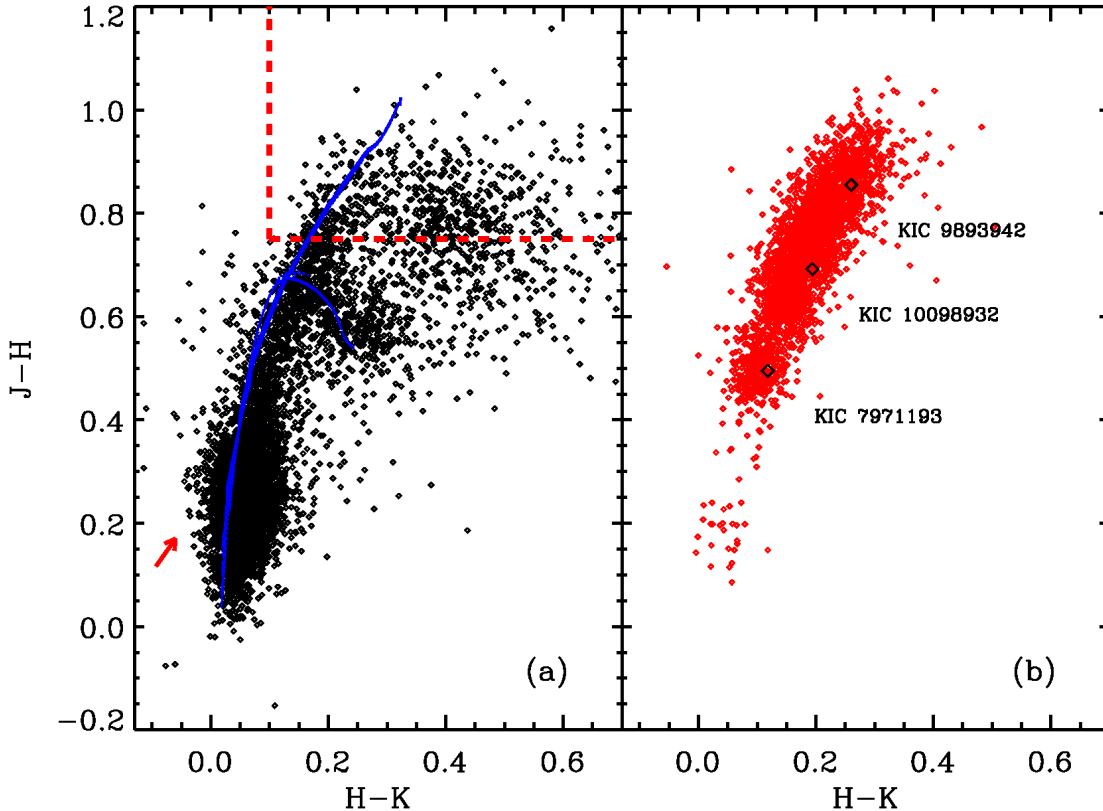


FIG. 2.— (a) 2MASS  $J-H$  versus  $H-K$  diagram for unclassified stars without asteroseismic detections. The blue line shows near-solar metallicity DSEP isochrones. The red arrow shows a typical reddening vector for  $A_V = 0.4$  mag. Note that temperature decreases from left to right and from bottom to top, with tracks for dwarfs and giant stars separating near  $J-H \gtrsim 0.7$  and  $H-K \gtrsim 0.1$ . The red-dashed box marks the color range for which stars were automatically classified as giant stars independent of an asteroseismic detection. (b) Same as left panel but for unclassified stars with an asteroseismic detection. Three examples of oscillating giants are marked, and their power spectra are shown in Figure 3.

ple to 11191 stars (2762 with asteroseismic detections). Figure 2a shows the unclassified sample without asteroseismic detections. The blue lines show near-solar metallicity DSEP isochrones described in Section 3. The observations are offset from the models due to reddening (see red arrow in Figure 2), illustrating the importance of extinction when deriving temperatures for unclassified *Kepler* stars. Note that dwarfs and giants separate for  $H-K \gtrsim 0.1$  (corresponding roughly to spectral type K5), with cooler dwarfs retaining a roughly constant  $J-H$  color. For hotter stars, however, the colors of dwarfs and giants overlap and an independent luminosity classification, e.g. from asteroseismology or spectroscopy, is required.

Figure 2b shows the same diagram but for unclassified stars with asteroseismic detections. As expected, asteroseismic detections are mainly found in cool stars in the top right section of the plot. Three typical examples of oscillating giants are marked, and their power spectra showing the presence of convection-driven oscillations are illustrated in Figure 3. Note that as giants become cooler and more luminous (larger  $J-H$  and  $H-K$  colors), their oscillation periods and amplitudes increase.

Notably, there is a significant fraction of stars in Figure 2a for which an asteroseismic detection would have been expected based on their 2MASS colors. Reasons for an asteroseismic non-detection in giants include that

the star is too cool and too evolved, resulting in pulsation periods that are too long for an unambiguous detection with 14 quarters of long-cadence data. Similarly, many unclassified stars have not been observed for the full mission duration, and hence the data provide lower frequency resolution. This discussion implies that a seismic detection is strong evidence that a star is a giant, but a seismic non-detection does not necessarily imply that a star is a dwarf. We therefore applied an additional color cut of  $H-K > 0.1$  and  $J-H > 0.75$  (see red box in Figure 2a) to identify giants based on 2MASS colors only. Using this procedure, we classify a total of 3302 giants ( $\log g < 3.5$ ) and 7889 subgiant or dwarf stars ( $\log g > 3.5$ ) in the unclassified sample.

To test our luminosity classifications, we restricted our sample to the same color-cut applied by Mann et al. (2012) ( $Kp-J > 2$ ,  $Kp < 14$ ) and found a total fraction of giant stars (selected using the asteroseismic classifications and 2MASS color cuts) of 90% using all stars, and 92% using only stars with a full set of *Kepler* data. This compares reasonably well to the giant fraction of 96% found by Mann et al. (2012) based on photometric and spectroscopic classifications. The remaining difference could be due to the fact that Mann et al. (2012) considered both classified and unclassified stars, or implies that our crude 2MASS color cut to identify giant stars is too conservative. We also note that, although

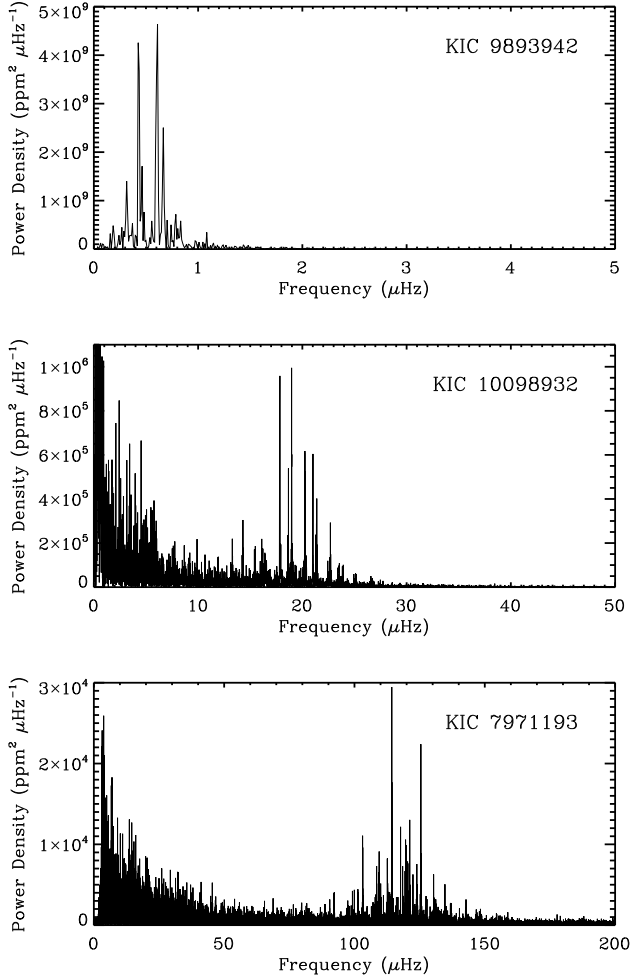


FIG. 3.— Power spectra of three unclassified stars marked in Figure 2b, showing clear power excess typical for convection-driven oscillations in giant stars. Note that more evolved giants with cooler temperatures (larger  $J-H$  and  $H-K$  in Figure 2b) oscillate with lower frequencies and larger amplitudes.

all seismic detections were checked by eye, it cannot be excluded that the unclassified seismic sample includes a small fraction of outliers which were erroneously classified as giants (for example due to blends). Future work including proper motion measurements will enable an improved giant-dwarf discrimination for *Kepler* targets.

### 5.2. Effective Temperatures

We determined effective temperatures for unclassified stars by comparing observed colors to theoretical values of the DSEP model grid described in Section 3. As shown in Figure 2, interstellar extinction is significant in this sample. To ensure consistency with the other *Kepler* targets, we adopted the same reddening model as applied in the KIC (see Section 2). For each star, we calculated the distance corresponding to each model  $J$ -band absolute magnitude and the apparent  $J$ -band magnitude, and determined the reddening at the distance and galactic latitude of the star. Note that we did not restrict reddening to a maximum value. This process was repeated until convergence in distance was reached. We adopted the reddening law by Cardelli et al. (1989), with

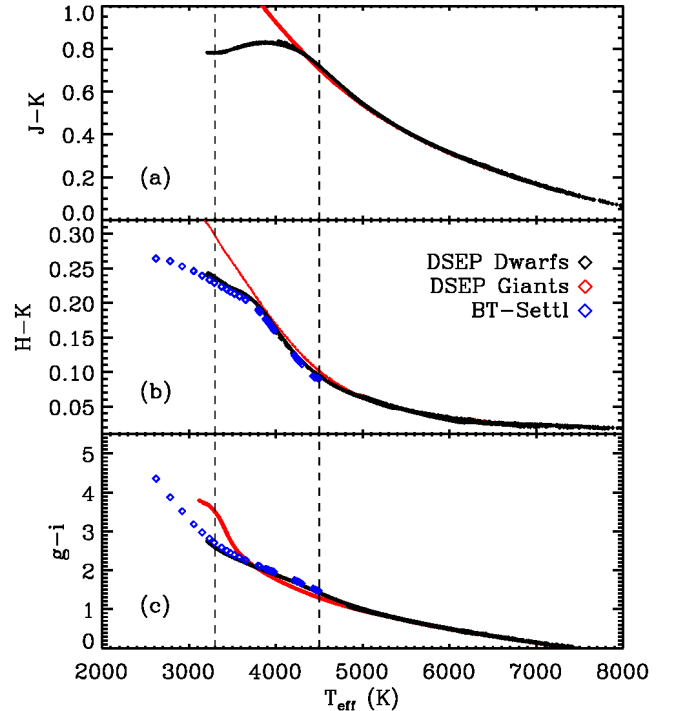


FIG. 4.— Relations between colors and effective temperatures for near solar-metallicity DSEP models for giants (red) and dwarfs (black), as well as solar-metallicity BT-Settl models (blue). Dashed lines denote the different regimes in which colors were used to derive temperatures: DSEP  $J-K$  for stars with  $T_{\text{eff}} \gtrsim 4500$  K, DSEP  $H-K$  and  $g-i$  for  $T_{\text{eff}} \sim 3300-4500$  K, and Bt-Settl  $H-K$  and  $g-i$  for  $T_{\text{eff}} \lesssim 3300$  K.

$A_V/A_J = 0.29$ . For each star, models were restricted to a given metallicity (see next Section).

The best-fitting model was identified by finding the closest matching model color to the observed color. Colors were matched to models depending on the spectral type of the star. Figure 4 shows the relation between  $J-K$ ,  $H-K$  and  $g-i$  to effective temperature for DSEP models of dwarfs (black) and giants (red).  $J-K$  provides the best thermometer for warmer stars with  $T_{\text{eff}} > 4500$  K. For cooler dwarfs, however,  $J-K$  becomes insensitive to  $T_{\text{eff}}$ .  $H-K$  shows some sensitivity, but only over a color span of  $\sim 0.1$  mag, which is relatively small compared to typical errors of 0.03 mag in 2MASS colors. We therefore adopted a third color based on  $g-i$  from the Kepler-INT survey (Greiss et al. 2012). Note that the Kepler-INT Sloan photometry is in the Vega system, which we converted into the AB system using the transformations by González-Solares et al. (2011). For stars between 3300 – 4500 K, temperatures were then derived from  $g-i$  when available, and otherwise from  $H-K$ . Finally, for the coolest dwarfs ( $< 3300$  K), we applied average polynomial relations from BT-Settl models, as described in Section 3.

To test the derived effective temperatures, we applied the same procedure to a subset of stars with available temperatures from Dressing & Charbonneau (2013) for dwarfs with  $T_{\text{eff}} < 4500$  K and P12 for dwarfs with  $T_{\text{eff}} > 4500$  K. The result of this comparison is shown in Figure 5a. For stars with  $T_{\text{eff}} < 4500$  K the agreement between the temperatures is excellent, implying

that Kepler-INT and KIC Sloan colors agree well for these stars. For hotter stars the agreement is good for  $T_{\text{eff}} \lesssim 5800$  K, but we observe an increasing systematic offset for hotter stars with DSEP temperatures being  $\sim 500$  K hotter than P12 temperatures at  $T_{\text{eff}} \sim 6500$  K. This offset is caused by the fact that a single color ( $J-K$ ,  $H-K$ , or  $g-i$ ) does not contain independent information on temperature and reddening (or  $\log g$ ), introducing a bias towards hotter, more luminous stars evolving off the main sequence. Since temperature and reddening are degenerate, more luminous and distant stars with greater reddening and lower  $\log g$  tend to be selected.

To correct for this bias and ensure consistency of the unclassified stars with the remaining sample, we apply an ad-hoc correction for hot stars with the same form as adopted by P12:

$$T_{\text{eff,cor}} = 5800 \text{ K} + 0.6(T_{\text{eff}} - 5800 \text{ K}), \quad (1)$$

for all stars with  $T_{\text{eff}} > 5800$  K.

Figure 5b shows a comparison of DSEP temperatures with temperatures from P12 for a sample of giant stars. We observe an offset, with DSEP temperatures being significantly ( $\sim 80$  K) cooler than the comparison values. This is consistent with the offset between temperatures derived from the  $J-K$  infrared flux method and temperatures based on Sloan colors discussed by P12. Since the offset is generally within the adopted uncertainties, we did not apply a systematic correction to temperatures of unclassified giant stars.

### 5.3. Surface Gravities and Metallicities

The determination of surface gravities and metallicities from broadband colors is a notoriously ill-posed problem due to strong degeneracies between fitted parameters. Our attempts to perform direct fits of observed colors to model colors quickly showed that many stars would be frequently matched with physical parameters that are unlikely to occur, such as massive subgiants in short-lived phases of stellar evolution.

Following B11, we therefore adopted priors on both surface gravity and metallicity. The  $\log g$  prior was constructed using stars in the Hipparcos catalog (van Leeuwen 2007) with distances  $< 100$  pc and fractional parallax uncertainties  $< 10\%$ . We first calculated a grid with a stepsize of 0.05 mag in  $(B-V)$  and 0.25 mag in  $M_V$  (calculated from the parallax assuming  $A_V = 0$ ) and counted the number of Hipparcos stars in each grid cell. For each DSEP model at a given metallicity, we then found the grid cell containing the  $(B-V)$  color and  $M_V$  magnitude of that model and assigned a prior probability corresponding to the number density of Hipparcos stars in that cell. Figure 6a shows the resulting  $\log g$  prior for a typical solar neighborhood metallicity. For the  $[\text{Fe}/\text{H}]$  prior we adopted the same analytic function as used for the KIC, which was constructed from metallicities in the Geneva-Copenhagen survey (Nordström et al. 2004). We note that the priors have been purposefully chosen to be very similar to those adopted by B11 to minimize biases between the unclassified stars and the remaining sample.

Incorporating these priors still resulted in distributions of stars that were unrealistically narrow, being confined to the peak of the prior distribution at a fixed temperature. This confirmed that the adopted colors ( $J-K$ ,

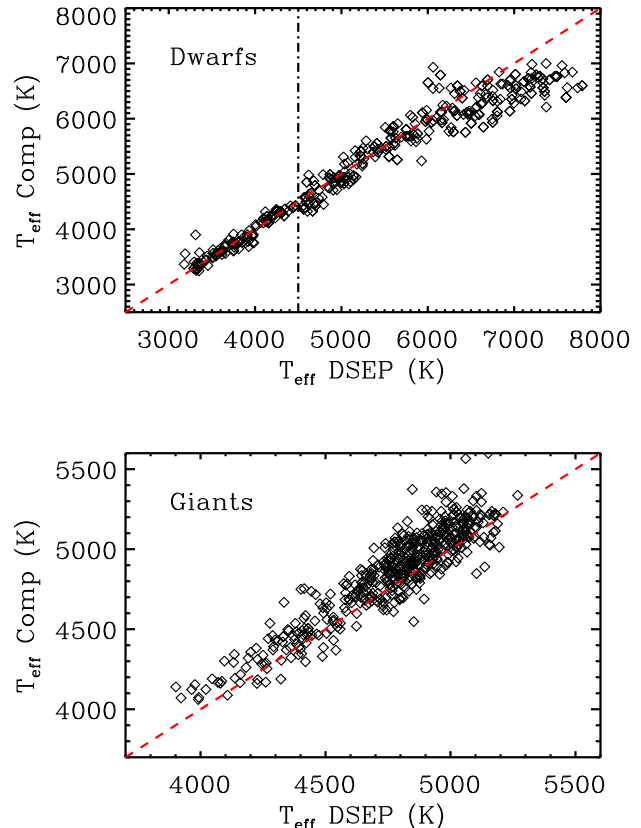


FIG. 5.— (a) Comparison of temperatures from Dressing & Charbonneau (2013) ( $T_{\text{eff}} < 4500$  K) and P12 ( $T_{\text{eff}} > 4500$  K) to temperatures derived from fitting single colors to DSEP models for dwarf stars. The red dashed line shows the 1:1 relation. (b) Same as panel (a) but for giant stars. The comparison sample is taken from P12.

$H-K$ ,  $g-i$ ) have little sensitivity to either  $\log g$  or  $[\text{Fe}/\text{H}]$ . To arrive at more realistic distributions, we calculated for each star a one-dimensional prior probability distribution in bins of 0.01 dex in  $\log g$  around a slice of 50 K centered on the  $T_{\text{eff}}$  determined in the previous section. We then drew a  $\log g$  value from this distribution with a probability corresponding to the prior value at a given  $\log g$ . The same procedure was applied to assign metallicities for a given star using the B11 metallicity prior. Note that for giant stars with asteroseismic detections, surface gravities were calculated from the measured frequency of maximum oscillation power, and hence only metallicities were assigned in this manner.

The resulting  $\log g$  versus  $T_{\text{eff}}$  distribution of the unclassified sample is shown in Figure 6b. By construction, the distribution in  $\log g$  closely follows the prior distribution shown in Figure 6a. *We stress that the procedure described in the previous paragraph means that  $\log g$  and/or  $[\text{Fe}/\text{H}]$  for unclassified stars are only statistically accurate, but are drawn from a prior probability on a star-by-star basis. The properties of these stars (except for temperatures) are therefore not suitable for scientific analyses on a star-by-star basis, and we strongly encourage follow-up observations for stars of particular interest (e.g. if planet candidates are detected).* Future efforts will improve the properties for these stars by using proper



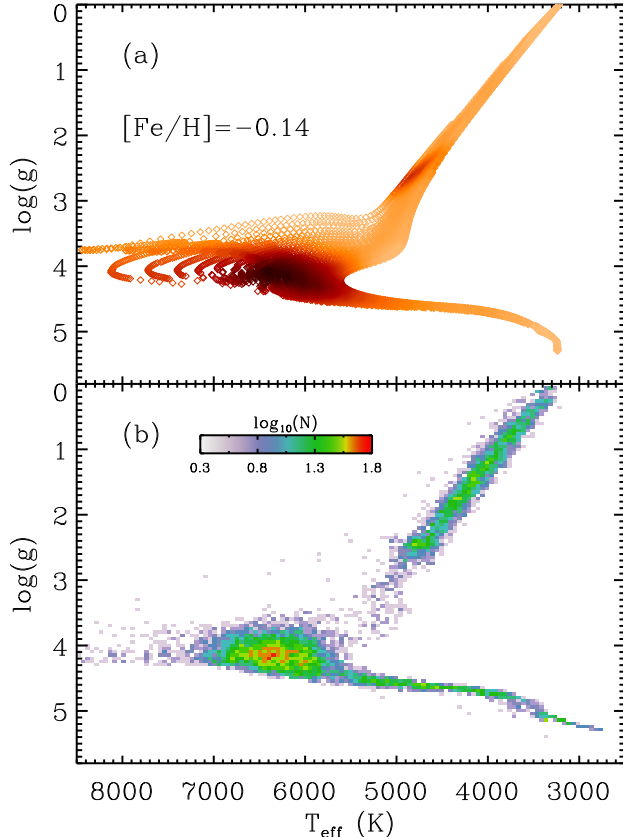


FIG. 6.— (a) Surface gravity versus effective temperature for DSEP models with a typical solar-neighborhood metallicity. Each model is color-coded according to the prior probability of observing a star in this parameter space, based on a distribution of stars in the Hipparcos catalog. Darker colors correspond to a higher prior probability. (b) Surface gravity versus effective temperature determined for the unclassified sample. Colors denote the relative logarithmic number density of stars as given in the legend.

motions or additional colors that contain independent information on surface gravities and metallicities.

Figure 6b also shows that there is a significant fraction of ultra cool dwarfs in the unclassified sample, which form a narrow band of stars with  $T_{\text{eff}} < 3300$  K. We recall that this discrete distribution is caused by the fact that we adopted typical stellar properties for ultra cool dwarfs based on polynomial fits to BT-Settl models (see Section 3). We note that  $\sim 100$  of these stars were matched to the coolest end of the BT-Settl polynomials due to very red  $H - K$  colors (see Figure 2), and were excluded from Figure 6b to avoid biasing the color scale. It is likely that a fraction of these ultra-cool dwarfs are giants, and we emphasize that the properties for these stars should be used with caution.

## 6. Q1–Q16 CATALOG

### 6.1. Uncertainties on Input Values

The procedures described in Sections 4 and 5 yielded input values for  $T_{\text{eff}}$ ,  $\log g$  and  $[\text{Fe}/\text{H}]$  for a total of 196,468 stars. Prior to fitting these constraints to models, uncertainties need to be specified for each input value. Since uncertainties quoted in the literature are heterogeneous, we adopted typical uncertainties on each

TABLE 2  
UNCERTAINTIES ADOPTED FOR THE INPUT PARAMETERS.

Method	$\sigma_{T_{\text{eff}}}$ (%)	$\sigma_{\log g}$ (dex)	$\sigma_{[\text{Fe}/\text{H}]}$ (dex)
Asteroseismology	—	0.03	—
Transits	—	0.05	—
Spectroscopy	2	0.15	0.15
Photometry	3.5	0.40	0.30
KIC	3.5	0.40	0.30

Note: An error floor of 80 K for spectroscopy and 100 K for photometry has been adopted for effective temperatures.

parameter depending on the observational method with which the parameter was derived.

Asteroseismic surface gravities have been shown to be accurate to at least 0.03 dex (Creevey et al. 2013; Morel & Miglio 2012; Hekker et al. 2013), which we adopted as a typical uncertainty independent of the evolutionary state of the star. Transit-derived densities have proven to be in good agreement with asteroseismic densities (e.g., Nutzman et al. 2011) but are based on an implicit assumption of circular orbits, and we hence assigned a slightly more conservative uncertainty of 0.05 dex. Typical spectroscopic uncertainties of 2% in  $T_{\text{eff}}$ , 0.15 dex in  $\log g$ , and 0.15 dex in  $[\text{Fe}/\text{H}]$  are based on the comparison of spectroscopic analyses with and without asteroseismic constraints (Huber et al. 2013a).

To estimate typical uncertainties for photometric methods, we have compared published results for a sample with combined spectroscopic and asteroseismic constraints to properties given in the KIC and P12 temperatures. The result is shown in Figure 7. The median and scatter of the residuals are  $+130 \pm 120$  K for the P12 temperatures (panel a),  $-130 \pm 140$  K for KIC temperatures (panel b),  $+0.13 \pm 0.33$  dex for KIC  $\log g$ , and  $-0.15 \pm 0.31$  for KIC  $[\text{Fe}/\text{H}]$ . Based on these residuals and previous estimates of uncertainties of KIC properties (e.g., Bruntt et al. 2011), we assigned uncertainties of 3.5% in  $T_{\text{eff}}$ , 0.4 dex in  $\log g$ , and 0.3 dex in  $[\text{Fe}/\text{H}]$ . We note that the P12 temperatures contain homogeneously derived uncertainties based on the quality of the input photometry. To preserve this information, uncertainties were calculated by adding a 2.5% systematic error in quadrature to the formal uncertainty given by P12. The typical adopted uncertainties are given in Table 2. Table 3 lists the reference key for the literature sources of the input values, and Table 4 lists the input values with adopted uncertainties for the whole catalog (see Section 6.5 for more details on provenances and reference keys).

### 6.2. Isochrone Fitting and Derived Uncertainties

The input values in Table 4 were fitted to the grid of DSEP isochrones to derive radii, masses, densities and luminosities. Matching observations to stellar isochrones is a non-trivial task, with important systematics such as the terminal age bias (Pont & Eyer 2004; Jørgensen & Lindegren 2005; Casagrande et al. 2011; Serenelli et al. 2013). We adopted an approach following Kallinger et al. (2010) and calculated for each star:

$$\mathcal{L}_X = \frac{1}{\sqrt{2\pi}\sigma_X} \exp\left(-\frac{(X_{\text{obs}} - X_{\text{model}})^2}{2\sigma_X^2}\right) \quad (2)$$

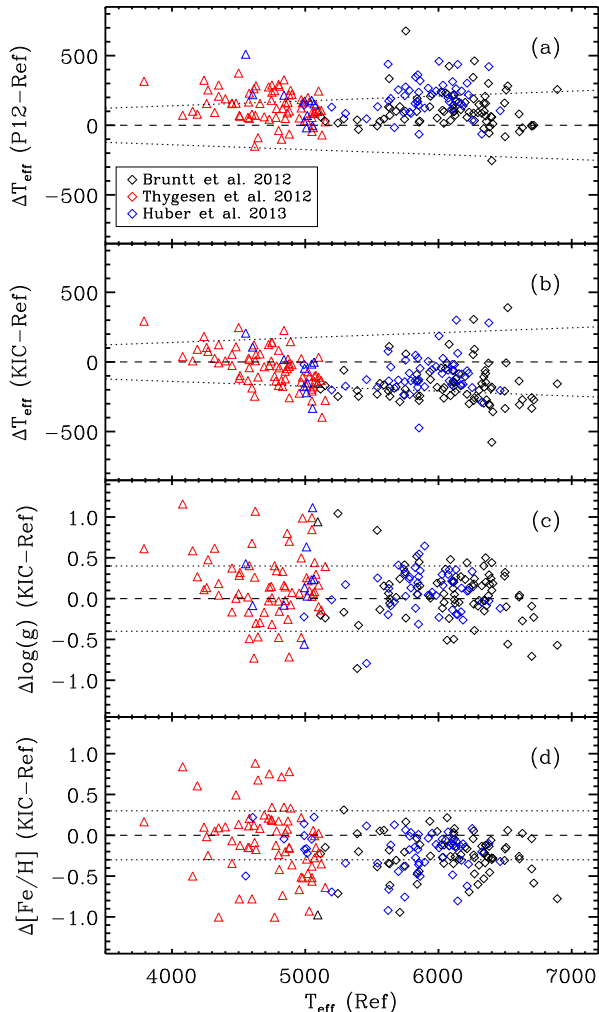


FIG. 7.— (a) Comparison of temperatures by P12 to temperatures derived for a “gold-standard” sample with constraints from asteroseismology and spectroscopy. Dotted lines correspond to the typical uncertainties adopted in this work. (b) Same as panel (a) but for KIC temperatures. (c) Same as panel (a) but for KIC surface gravities. (d) Same as panel (a) but for KIC metallicities.

where  $X = \{T_{\text{eff}}, \log g, [\text{Fe}/\text{H}]\}$  are assumed to be independent Gaussian observables. The combined likelihood is:

$$\mathcal{L} = \mathcal{L}_{T_{\text{eff}}} \mathcal{L}_{\log g} \mathcal{L}_{[\text{Fe}/\text{H}]} . \quad (3)$$

For each parameter, Equation 3 yields a probability distribution that was used to calculate the best-fit, median and 68% (1- $\sigma$ ) intervals.

The reported value for each stellar property in the catalog corresponds to the best-fitting model, which was determined by maximizing Equation (3). To specify an error bar as a single number (as required by the *Kepler* planet-detection pipeline), we reported the largest distance of the best fit to the upper or lower limit of the 1- $\sigma$  interval around the median of the probability distribution. For highly asymmetric distributions this procedure results in conservative estimates, as further discussed below. We have also derived a second set of uncertainties

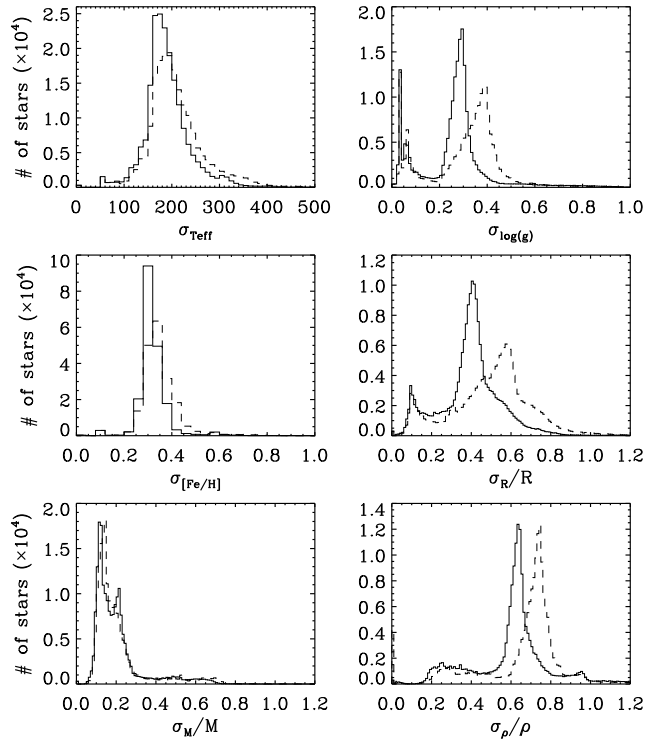


FIG. 8.— Histograms of uncertainties in  $T_{\text{eff}}$ ,  $\log g$ ,  $[\text{Fe}/\text{H}]$ ,  $R$ ,  $M$  and  $\rho$  for the full sample. Solid lines show uncertainties based on the 1- $\sigma$  interval closest to the best-fit, and dashed lines show uncertainties based on the central 1- $\sigma$  interval (see text). Note that we show absolute uncertainties for  $T_{\text{eff}}$ ,  $\log g$ , and  $[\text{Fe}/\text{H}]$ , and relative uncertainties for  $R$ ,  $M$  and  $\rho$ .

by calculating the largest difference of the best-fit value to the lower or upper limit of the closest 1- $\sigma$  interval around the best-fit.

Figure 8 shows histograms of the derived uncertainties for  $T_{\text{eff}}$ ,  $\log g$ ,  $[\text{Fe}/\text{H}]$ ,  $R$ ,  $M$  and  $\rho$ . As expected, the uncertainties on  $T_{\text{eff}}$ ,  $\log g$ ,  $[\text{Fe}/\text{H}]$  largely follow the distribution of uncertainties adopted on the input parameters. Uncertainties based on the 1- $\sigma$  interval around the median (dashed lines) are systematically larger than estimates based on the 1- $\sigma$  interval around the best-fit (solid lines) for higher input uncertainties in  $\log g$ , radius and density. This is due to asymmetric probability distributions for main-sequence stars whose initial  $\log g$  estimates were based on photometry: assuming a 0.4 dex uncertainty, the finite extent of the isochrone grid causes a sharp cut-off at large  $\log g$  values. For smaller fractional uncertainties the distributions become more symmetric, and the two uncertainty estimates agree better. Temperature and mass mostly yield symmetric distributions, and so this effect does not arise. Median uncertainties in radius for the full sample over both methods span 40 – 55% in radius, and 60 – 75% in density. For stellar mass the typical uncertainty is  $\sim 20\%$ , confirming that mass is mainly constrained by  $T_{\text{eff}}$  and less affected by large uncertainties in  $\log g$ . Based on the above discussion, we conclude that the uncertainty estimates based on the central 1- $\sigma$  interval (which were used in the *Kepler* planet-detection pipeline) are probably conservative, especially for main-sequence stars whose input surface gravities were based on photometry.

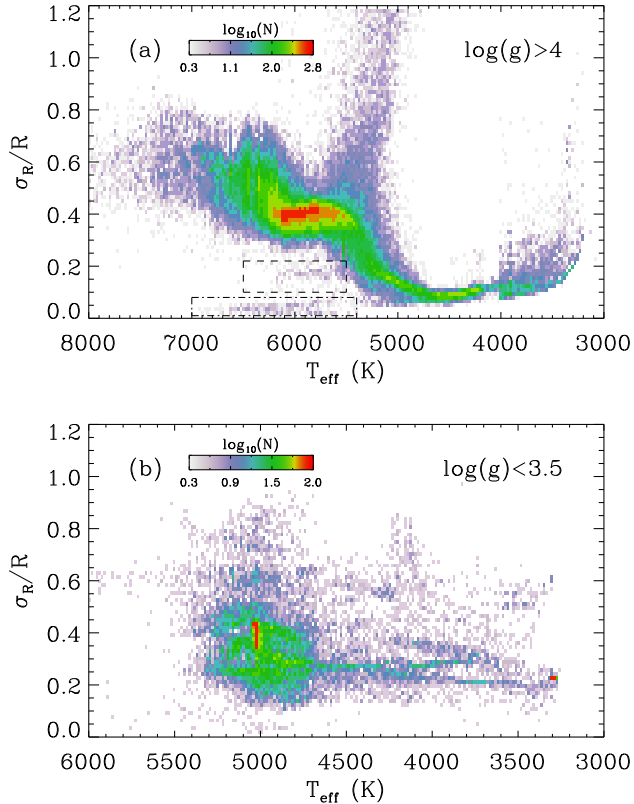


FIG. 9.— (a) Relative radius uncertainty as a function of effective temperature for dwarfs ( $\log g > 4$ ). Colors denote the relative logarithmic number density of stars as given in the legend. The dashed-dotted and dashed boxes mark stars with surface gravities based on asteroseismology and spectroscopy, respectively. (b) Same as panel (a) but for giants ( $\log g < 3.5$ ). Note that the majority of these stars have asteroseismic  $\log g$  measurements.

It is informative to analyze the relative radius uncertainty as a function of effective temperature, as shown in Figure 9a (see also Gaidos & Mann 2013). Note that we show the uncertainties based on the  $1\text{-}\sigma$  interval around the best-fit here, but the comparison is qualitatively similar for the uncertainties based on the  $1\text{-}\sigma$  interval around the median. For G-type dwarfs the median radius uncertainty based on photometry is 40%, increasing to higher values for more massive dwarfs. The “band” of points with large uncertainties at  $T_{\text{eff}} \sim 5000\text{K}$  is due to K-dwarfs in the “No-Man’s-Land” zone (see Section 8), which have highly bimodal radius distributions reaching from the main-sequence to the subgiant branch. For even cooler stars, this subgiant degeneracy disappears, and the much slower evolution of stars constrains the radius to typical uncertainties of 20%. We emphasize that these uncertainties do not include potential systematic errors in the models, which can be significant particularly for cool dwarfs (see, e.g., Boyajian et al. 2012). Dashed-dotted and dashed boxes highlight the smaller subset of stars with constraints from asteroseismology and spectroscopy, respectively. As expected, the relative uncertainties are smaller, making targets with asteroseismic measurements the best characterized stars in the *Kepler* field.

Figure 9b shows the relative radius uncertainty distribution for giant stars. Stars with asteroseismic measure-

ments dominate this sample, with typical relative uncertainties in radius of  $\sim 30\%$ . We emphasize that such uncertainties are atypically large since we have only used asteroseismic constraints on  $\log g$  and ignored any information on the mean density, which is typically much better constrained. Ongoing projects aimed at combining APOGEE H-band spectra (Eisenstein et al. 2011) with seismic constraints for Kepler giants (the APOKASC project, see Mészáros et al. 2013; Pinsonneault et al. 2014) will soon provide much improved radii, masses and ages of oscillating giants in the *Kepler* field.

### 6.3. Comparisons with Published Radii and Masses

We have compared our catalog results with published radii and masses derived using different methods and models. Figure 10 shows a comparison for confirmed *Kepler* planet host stars taken from the NASA exoplanet archive<sup>27</sup> (black), as well as the larger sample of planet-candidate host stars by Buchhave et al. (2012) (red) for stars with relative uncertainties better than 20%. In both cases the majority of the radii and masses were derived using Yonsei-Yale (YY) evolutionary tracks (Yi et al. 2001). Overall the residuals show an offset of 1% with a scatter of 7% for radius and an offset of 3% with a scatter of 6% for mass. These offsets, which are more pronounced for the sample by Buchhave et al. (2012), are likely due to differences in the interior models and assumptions of uncertainties on the input values. We also observe systematic differences at the low-mass end ( $\lesssim 0.8M_{\odot}$ ), resulting in a “kink” with higher DSEP masses and radii between  $\sim 0.6 - 0.8M_{\odot}$ , and lower DSEP masses and radii for  $\lesssim 0.6M_{\odot}$ . This is consistent with systematic differences between DSEP and YY models due to different equations of state adopted for low-mass stars (Dotter et al. 2008).

As an additional test we calculated radii and masses from  $T_{\text{eff}}$ ,  $\log g$  and  $[\text{Fe}/\text{H}]$  using the empirical relations by Torres et al. (2010), which were calibrated using a large sample of detached eclipsing binary systems. A comparison with the radii and masses derived in this work is shown in Figure 11 for the mass range in which the Torres et al. (2010) relations are valid. We observe that the catalog radii and masses are systematically smaller by  $\sim 5\%$  than the empirical values. As noted by Torres et al. (2010), a similar offset in mass is found when comparing empirically calculated values to YY isochrone values by Valenti & Fischer (2005), or when using observed values for the Sun. Importantly, the offset to the Q1–Q16 catalog does not vary with stellar mass and radius, and is typically well within the quoted uncertainties.

### 6.4. Catalog Overrides

The primary motivation for fitting  $T_{\text{eff}}$ ,  $\log g$  and  $[\text{Fe}/\text{H}]$  to a single set of isochrones was to ensure a homogeneous treatment for all stars. However, methods such as asteroseismology provide significantly better constraints on other stellar properties such as the mean stellar density. Hence, omitting such additional information can yield significantly less accurate stellar radii and masses. More importantly, some of the

<sup>27</sup> <http://exoplanetarchive.ipac.caltech.edu/>

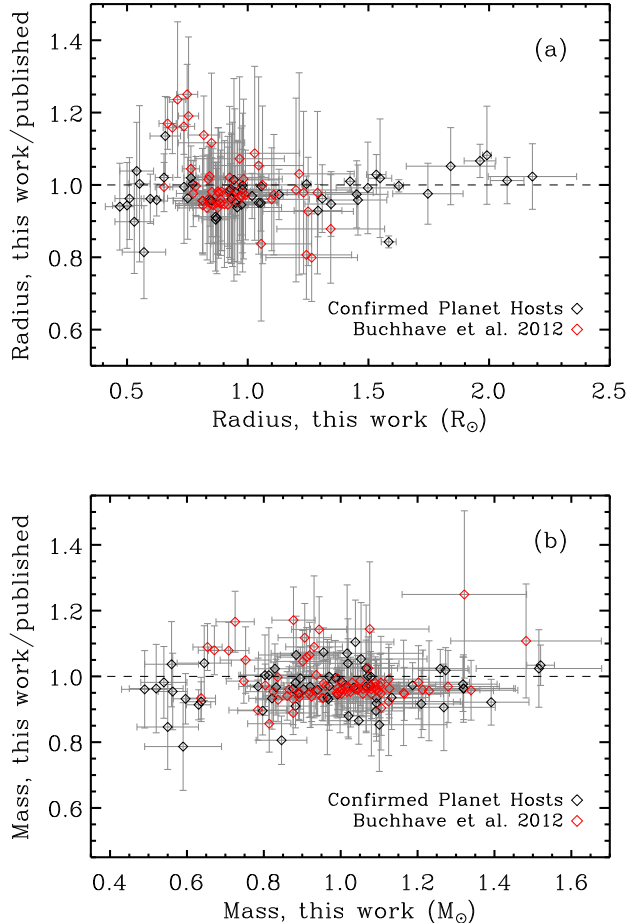


FIG. 10.— (a) Fractional difference between published radii and masses and values derived in this work for confirmed planet host stars (black) and planet-candidate host stars analyzed by Buchhave et al. (2012) (red). Only stars with relative uncertainties better than 20% are shown. (b) Same as panel (a) but for stellar masses.

studies used in the consolidation of literature values adopted the same models as in this study, hence removing the need to re-fit the parameters to ensure consistency with the remaining sample. For these reasons, we have adopted literature values for all stars with published masses, radii and densities that are based on DSEP models. These studies include Dressing & Charbonneau (2013) and Muirhead et al. (2012a) for M dwarfs, and Chaplin et al. (2014) and Huber et al. (2013a) for F-G dwarfs with asteroseismic measurements. Note that the latter two studies used a variety of models including DSEP, hence providing more robust estimates of uncertainties on stellar properties.

### 6.5. Final Catalog Description

The complete Q1–Q16 star properties catalog is presented in Table 5. For each star we list the best-fitting  $T_{\text{eff}}$ ,  $\log g$ ,  $[\text{Fe}/\text{H}]$ , radius, mass and density, together with the uncertainty based on the  $1\text{-}\sigma$  interval around the best fit, as described in Section 6.2<sup>28</sup>. For stars with pub-

<sup>28</sup> We note that the procedure also yielded additional parameters (such as distances) which, however, were omitted from this catalog

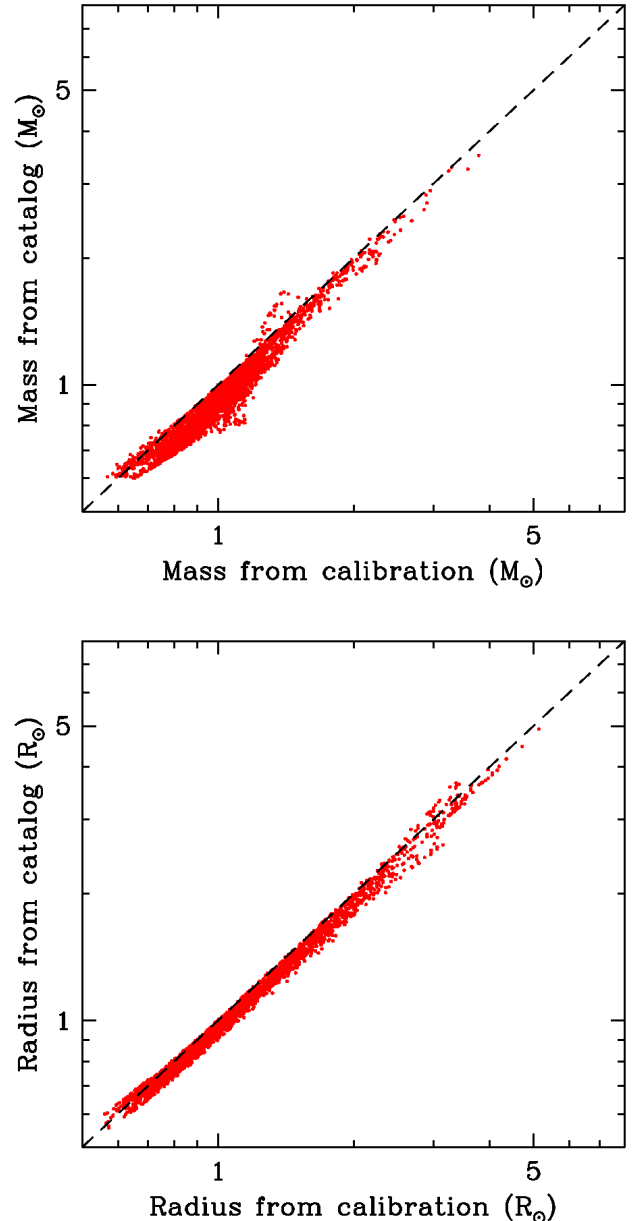


FIG. 11.— (a) Stellar masses in the Q1–Q16 catalog compared to empirical values calculated from  $T_{\text{eff}}$ ,  $\log g$  and  $[\text{Fe}/\text{H}]$  using the relations by Torres et al. (2010). The dashed line shows the 1:1 relation. (b) Same as panel (a) but for stellar radii.

lished masses, radii and densities based on DSEP models, stellar properties and uncertainties as given in the literature are listed (see Section 6.4). Each entry contains provenance flags specifying the origin of the input  $T_{\text{eff}}$ ,  $\log g$ , and  $[\text{Fe}/\text{H}]$ . The provenance consists of a three letter abbreviation of the method used to derive the parameter and a number specifying the reference from which the parameter was adopted. The abbreviations are as follows (see also Section 4):

- AST = Asteroseismology

due to the large uncertainties. Additional parameters for subsets of stars are available on request, and will be added to future updates of the catalog.

- TRA = Transits
- SPE = Spectroscopy
- PHO = Photometry
- KIC = Kepler Input Catalog

In addition to the provenances for  $T_{\text{eff}}$ ,  $\log g$ ,  $[\text{Fe}/\text{H}]$ , Table 5 also lists a provenance for the source of interior parameters ( $R$ ,  $M$  and  $\rho$ ). The abbreviations are as follows:

- DSEP = Derived from the Dartmouth Stellar Evolution Program Models
- MULT = Derived from multiple evolutionary tracks/isochrones, including DSEP

Note that entries specifying DSEP without a reference number correspond to values derived with the model grid presented in this work. Interior model flags with reference numbers correspond to entries which were replaced by published solutions (see Section 6.4).

The reference key is provided in Table 3. Using the three letter abbreviations described above and the reference number, each parameter is directly traceable to a single reference and method, and subsets of stars can be filtered according to individual methods or references. For example, restricting the sample to provenances containing SPE+AST+SPE for  $T_{\text{eff}}+\log g+[\text{Fe}/\text{H}]$  will extract the “gold-standard” sample of stars with combined asteroseismic and spectroscopic constraints.

The stellar properties presented in this paper have been adopted in the Q1–Q16 transit detection run described in Tenenbaum et al. (2014). We note that the uncertainties adopted in that run (and hence displayed in *Kepler* pipeline products such as data validation reports at the NASA Exoplanet Archive) differ from those reported in Table 5 for reasons described in Section 6.2. We emphasize, however, that these uncertainties are not currently used in the *Kepler* pipeline, and hence this difference does not affect the results in the data validation reports. We also note that targets that have only been observed in Q0 (commissioning) are not analyzed in the transit detection run, and hence have also not been included in this catalog. Additionally,  $\sim 2000$  stars which are unclassified in the KIC and do not have AAA-quality 2MASS photometry remain unclassified in this work, and hence have not been included in the catalog (see Section 5).

## 7. COMPARISON TO PREVIOUS CATALOGS

Systematic revisions of stellar properties for *Kepler* targets have previously been performed for the Q1–Q6 planet-candidate catalog (Batalha et al. 2013). Following a similar methodology as to this work, constraints from spectroscopic follow-up observations and the KIC were fitted to YY models to reduce well-known biases that are present in the KIC. The procedure was subsequently extended to a larger sample of *Kepler* targets and the revised properties were adopted for the *Kepler* transit detection runs producing the Q1–Q8 (Burke et al. 2014) and Q1–Q12 (Tenenbaum et al. 2013; Rowe et al. 2014) planet-candidate catalogs.

Figure 12 compares radii as a function of effective temperature for the *Kepler* target sample as derived in this

work to the catalog used for the Q1–Q12 transit detection run. Note that we compare stellar radii because this is the most important property in the context of exoplanet transits. The Q1–Q12 sample consists of three categories, which are marked with different provenances in the NASA Exoplanet Archive: P12 temperatures for a fixed metallicity ( $[\text{Fe}/\text{H}] = -0.2$ ) which were combined with KIC  $\log g$  values and fitted to YY tracks (provenance “Pinsonneault”, 80% of the sample), original KIC values (provenance “KIC”, 13% of the sample) and unclassified stars which were assumed to have solar values (provenance “Solar”, 7% of the sample). Note that the latter category was excluded from Figure 12 to avoid biasing the color scale.

Inspection of Figure 12 shows several important differences between the two catalogs. First, cool M dwarfs now extend to much lower temperatures and radii due to the improved coverage of DSEP compared to YY models and the KIC in this parameter regime (Dressing & Charbonneau 2013). Second, K dwarfs with KIC radii  $\sim 1R_{\odot}$  as well as G dwarfs with KIC radii  $\sim 0.5R_{\odot}$  (“No-Man’s-Land” stars) are now forced to models compatible with 0.25–15 Gyr isochrones, resulting in smaller radii for the former and larger radii for the latter. For K dwarfs this results in a sharp boundary corresponding to the oldest isochrone for cool stars. Third, the upper red giant branch in the Q1–Q16 catalog is now more populated, with stars reaching up to and beyond  $100R_{\odot}$ . The majority of these were unclassified stars which have now been identified as luminous giants.

Figure 13 shows the ratio between radii presented in this catalog and those in the Q1–Q12 catalog as a function of temperature. The median ratio for F–G stars is close to one with a scatter of about 10%. This scatter is mostly due to the constant metallicity of  $[\text{Fe}/\text{H}] = -0.2$  assumed in the Q1–Q12 catalog, whereas for the Q1–Q16 catalog we adopted a metallicity distribution. For certain temperature ranges, large differences in radius can be observed. First, the two “bands” of stars with radii up to a factor two or more larger than in the previous catalog are due to unclassified stars that were previously assumed to have solar properties, but have now been classified either as giants ( $T_{\text{eff}} \sim 5000$  K) or stars evolved off the main-sequence ( $T_{\text{eff}} \sim 6000$  K), as well as giants for which KIC  $\log g$  values were systematically higher than those determined from asteroseismology ( $T_{\text{eff}} \sim 5000$  K). Second, K dwarfs ( $\sim 4000 - 5000$  K) which were previously fitted to YY isochrones in the Q1–Q12 catalog now have radii that are up to  $\sim 10\%$  larger due to model-dependent differences between YY and DSEP models (see Section 6.3). Third, a large fraction of M dwarfs ( $< 4000$  K) have radii that are smaller than in the Q1–Q12 catalog. These are predominantly stars for which radii were adopted from the original KIC, and have now been revised with models more appropriate for cool dwarfs. Remarkably, for the coolest dwarfs the updated radii are up to 90% smaller than those used in the Q1–Q12 catalog.

We emphasize that the large changes in the radii of some Kepler targets will have a significant influence on the inferred radii of planet candidates (particularly if the host stars were previously unclassified), as well as estimates of planet-occurrence rates. The stellar radii presented here should allow an improved identification of false-positive planet candidates, as well as the identifi-

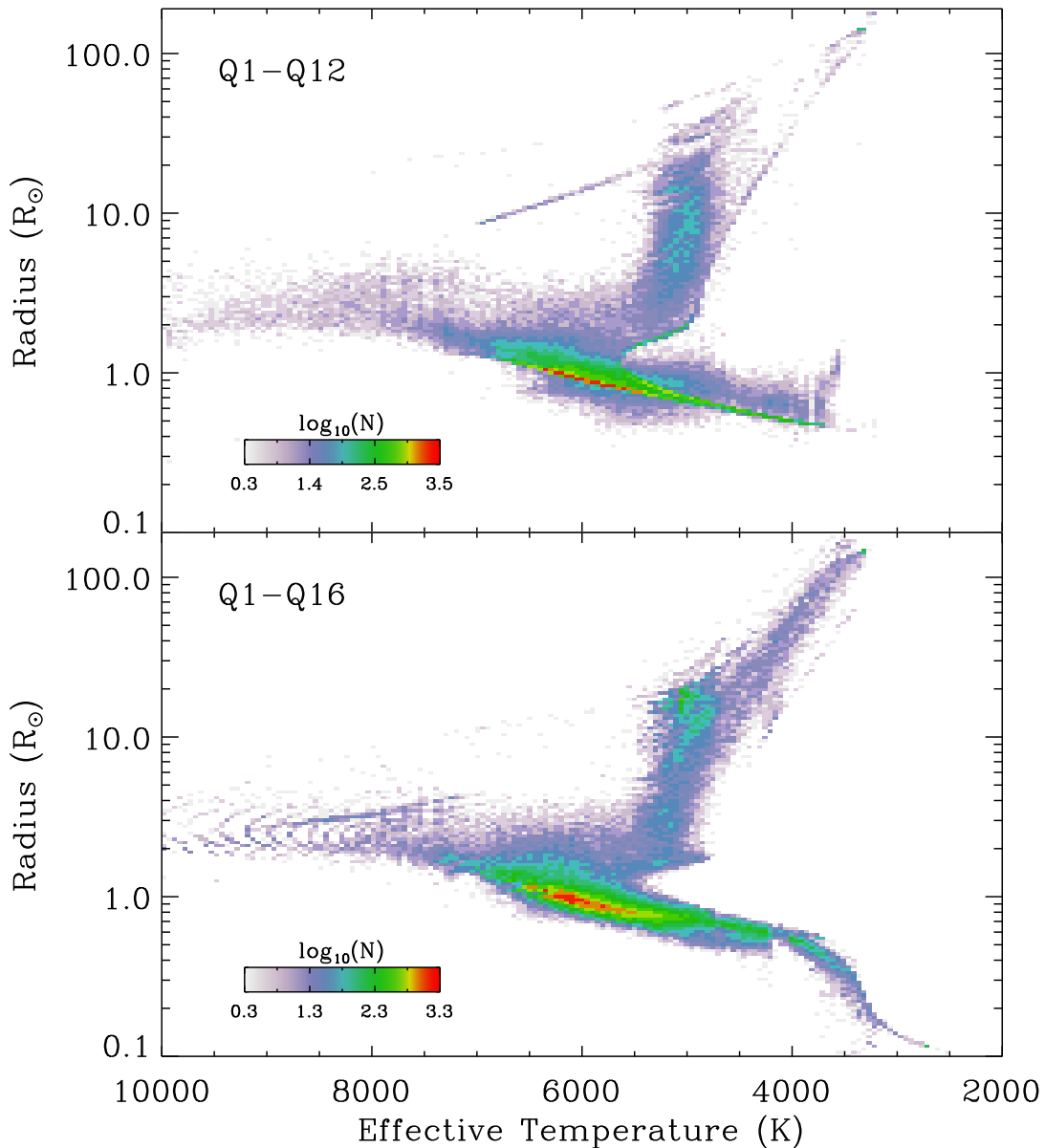


FIG. 12.— Radius versus temperature for the *Kepler* target sample in the Q1–Q12 star properties catalog (top panel) and the catalog presented here (bottom panel). Colors denote the relative logarithmic number density of stars as given in the legend.

cation of interesting candidates orbiting in or near the habitable zones of their host stars.

## 8. CATALOG SHORTCOMINGS

The methodology in this work inevitably results in a number of shortcomings that need to be considered when using this catalog.

### 8.1. General Considerations

The general trends and biases in the sample can be summarized as follows:

- For  $\sim 70\%$  of all stars the input  $\log g$  and  $[\text{Fe}/\text{H}]$  values are still based on the KIC, and hence any

biases in these values (for example potential systematic overestimates of  $\log g$  for G-type dwarfs, see Verner et al. 2011; Everett et al. 2013) will be included into the Q1–Q16 catalog.

- The catalog is based on literature values from a variety of techniques, and hence includes systematic offsets between these different methods. For example, spectroscopic temperatures are well known to be systematically offset from photometric temperatures (see Figure 7).
- Surface gravities and metallicities for dwarfs and metallicities for giants that are unclassified in the KIC are valid in a statistical sense only, but are

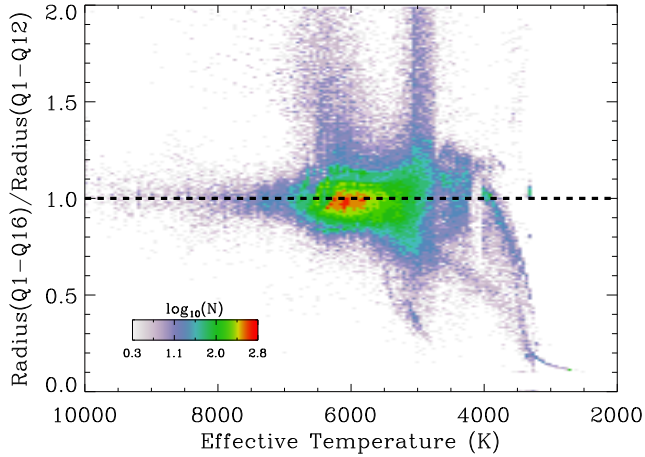


FIG. 13.— Ratio of radii in the current catalog and the radii in the Q1-Q12 catalog as a function of effective temperature. Colors denote the relative logarithmic number density of stars as given in the legend.

not accurate on a star-to-star basis. Follow-up observations of these stars are highly recommended, especially if a planet-candidate is detected. Stellar properties of ultra cool dwarfs that were previously unclassified in the KIC should also be treated with caution.

- The adopted isochrone grid does not include He-core burning models for low-mass stars, and hence radii, masses and densities for red giant stars are systematically biased as they are more frequently matched to higher-mass models which include He-core burning models. To derive realistic radii and masses for red giants, it is highly recommended to repeat the isochrone or evolutionary track fits using grids which include He-core burning models.
- Uncertainties on stellar properties adopted in the Q1-Q16 transit detection run (Tenenbaum et al. 2014) are conservative estimates and may be overestimated for cases with very asymmetric probability distributions. This particularly applies to F-K dwarfs. The uncertainties presented in this paper provide improved estimates which should be unaffected by these biases. We note, however, that lower or upper  $1-\sigma$  intervals may be significantly underestimated for stars near the edge of the model grid.
- The isochrone fitting method adopted in this study ignores priors on stellar evolution such as an initial mass function or star formation history. Potential biases introduced by e.g. different evolutionary speeds of stars and different densities of models in certain parameter ranges are not yet considered.

### 8.2. “No-Man’s-Land” Stars

In their revision of properties of *Kepler* planet-candidate host stars, Batalha et al. (2013) identified two groups of stars with KIC surface gravities and temperatures that were incompatible with YY isochrones. These two groups, namely G-type dwarfs with  $\log g \sim 5$  and K

dwarfs with  $T_{\text{eff}} \sim 5000\text{K}$  and  $\log g \sim 4.2$ , were subsequently matched to the closest YY isochrone. Lacking any further observational information, the fitting procedure in this work results in a similar classification of these “No-Man’s-Land” stars.

To test the accuracy of this procedure, we selected stars in the KIC that are either cooler than a 14 Gyr isochrone with  $[\text{Fe}/\text{H}] = +0.5$  dex, or have a  $\log g$  that is higher than the highest  $\log g$  of a 1-Gyr isochrone with  $[\text{Fe}/\text{H}] = -2.09$  dex. Isochrones for this selection were taken from the BaSTI grid (Pietrinferni et al. 2004). While these age and metallicity cuts are somewhat arbitrary, they do not affect the general conclusions presented in this section. The selected sample was then cross-matched to the SEGUE catalog of spectroscopic classifications (Yanny et al. 2009), yielding an overlap of 140 stars (the total overlap between the KIC and SEGUE includes  $\sim 2220$  stars, none of which are *Kepler* targets). The comparison of temperatures and surface gravities for this sample is shown in Figure 14. As expected, stars generally move away from the “No-Man’s-Land”, with most high-gravity G-type dwarfs moving closer to the main-sequence. For the cool “No-Man’s-Land” sample, stars move in roughly equal numbers towards the main-sequence or the subgiant branch. Notably, some of the stars are identified as giants in the SEGUE classification. Additionally, a considerable number of SEGUE classifications remain in the “No-Man’s-Land” zone. Such targets may correspond to stars with unusual properties or rare evolutionary stages, such as merger products, unresolved binary stars, pre-main-sequence stars, or cases in which the medium-resolution SEGUE spectra ( $R \sim 2000$ ) did not yield a reliable classification.

While the comparison shows that moving stars to the nearest isochrone qualitatively yields improved stellar properties, it is clear from Figure 14 that for some stars such a procedure can in fact yield a *larger* discrepancy to spectroscopic classifications than initially given in the KIC. We stress that stellar radii for some of these targets may be considerably over- or underestimated.

## 9. CONCLUSIONS AND FUTURE PROSPECTS

We have presented revised properties for 196,468 stars observed by the NASA *Kepler* mission. The main objective of the catalog was to consolidate the large amount of stellar characterization work that has been published since the launch of *Kepler* based on different observation techniques such as asteroseismology, spectroscopy, photometry and exoplanet transits. Additionally, we estimated the parameters of stars previously unclassified in the KIC, including 2726 new oscillating red giant stars. The two samples were then combined and homogeneously fit to a dense grid of isochrones to derive improved estimates (including uncertainties) of temperatures, radii, masses and densities for *Kepler* target stars. The revised radii and temperatures in the catalog should allow an improved identification of false-positive planet candidates and planet candidates orbiting in or near the habitable zones of their host stars. We emphasize that the present catalog still includes a number of important caveats, as summarized in Section 8.

Ideally, a catalog of *Kepler* targets should provide the most accurate stellar properties on a star-by-star basis, while at the same time being as homogeneous as possi-

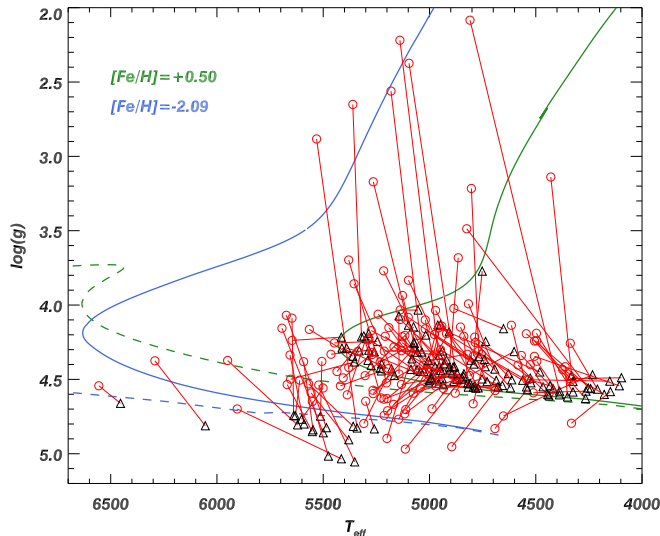


FIG. 14.— Surface gravity versus effective temperature for a sample of KIC stars in the “No-Man’s-Land” zone (black triangles). Solid and dashed lines show 14 Gyr and 1 Gyr isochrones for two extreme metallicity ranges taken from the BaSTI grid (Pietrinferni et al. 2004), which were used to select the sample. Red circles show the position of the same sample as determined from medium-resolution SEGUE spectra. Red lines connect the KIC and SEGUE values for each individual star.

ble. The present catalog is somewhat of a compromise between accuracy and homogeneity: on one hand, using literature values should provide the best possible properties for a given star, while fitting  $T_{\text{eff}}$ ,  $\log g$  and  $[\text{Fe}/\text{H}]$  to a single large grid of isochrones technically ensures that the whole sample is internally self-consistent. On the other hand, combining different observational techniques inevitably introduces systematic effects that are incorporated into the catalog, and are nearly impossible to quantify a posteriori. Compared to the KIC the Q1–Q16 catalog is significantly more heterogeneous, which should be kept in mind for studies vulnerable to biases such as planet occurrence rates. However, given the known biases towards unphysical stellar properties in the KIC, especially for late-type dwarfs, the approach for the Q1–Q16 catalog will likely still be an improvement despite the fact that some of the input sources are not homogeneous.

Several promising prospects exist to improve further on the current catalog. First, it will be essential to provide star properties that are independent of KIC-derived properties by refitting the broadband photometry to stellar models (e.g., Dressing & Charbonneau 2013; Gaidos 2013). As partially shown for the unclassified stars in this study (see Section 5), the newly available Kepler-INT photometry, which covers nearly 98% of all *Kepler* targets, holds great promise to complement the available KIC *griz* colors. In particular, the availability of *U* and *z* band photometry, which is mostly incomplete in the KIC, will be essential for improved constraints on reddening, surface gravity and metallicity.

Improved reddening models will also be essential to derive accurate properties based on broadband photometry. The APOKASC collaboration (Pinsonneault et al. 2014) has collected H-band spectra for thousands of oscillating red giants, which can be combined to derive reddening-

independent estimates of  $T_{\text{eff}}$ ,  $\log g$  and  $[\text{Fe}/\text{H}]$ . Given the large number of oscillating red giants spread across the *Kepler* field, this should in principle allow the construction of an empirical reddening map. Furthermore, independent reddening estimates can be derived using WISE near-infrared photometry (Wright et al. 2010). Large-scale spectroscopic surveys such as APOGEE will also allow measurements of the metallicity distribution of stars in the *Kepler* field, which may be significantly different than the solar neighborhood.

Asteroseismology of yet unidentified red giants using long-cadence data will continue to play a major role for characterizing *Kepler* targets. In particular, a complete census of all giants observed by *Kepler* will be of prime importance, for example by using the detection of oscillations in long-cadence data to identify cool stars which might have been misclassified as dwarfs in the KIC. Additionally, Figure 1 shows that a significant number of stars with KIC  $\log g < 3.5$  are not yet included in the asteroseismic sample, potentially indicating a significant fraction of misclassified giant stars in the KIC that are subgiants or dwarf stars.

One of the most important aspects for future catalogs will be the availability of a control sample of stars with well-determined properties. Such a control sample will include stars with asteroseismic properties, as well as the large number of Kepler Objects of Interest with spectroscopic follow-up observations obtained by the Kepler Community Follow-Up Program. A particularly promising new technique is the determination of empirical surface gravities from the measurement of granulation on time scales accessible with *Kepler* long-cadence data (Mathur et al. 2011; Bastien et al. 2013). This new technique has great potential for measuring accurate surface gravities for a large number of stars, especially if the calibration can be extended to a larger parameter space than currently available. Based on this potentially large and diverse control sample, homogenous transformations from broadband colors to stellar properties for the full sample of *Kepler* targets can be calibrated, resulting in a catalog which is both accurate and homogeneous.

While the *Kepler* mission has been a spectacular success for the detection of exoplanets and stellar astrophysics in general, our understanding of the underlying stellar population of the target sample is still limited. Using new and improved techniques and follow-up observations, a major future goal will be to improve the characterization of all *Kepler* targets to maximize the science output both for galactic stellar population studies and for studies of exoplanet occurrence rates and populations.

#### ACKNOWLEDGMENTS

We thank Lars Buchhave, Bill Cochran, Jonas Debosscher, Joris De Ridder, Mathieu Havel, Ulrich Kolb, Dave Latham, Mikkel Lund, Phil Muirhead and Angie Wolfgang for helpful discussions and comments. Funding for the *Kepler* Mission is provided by NASA’s Science Mission Directorate. D.H. acknowledges support by an appointment to the NASA Postdoctoral Program at Ames Research Center, administered by Oak Ridge Associated Universities through a contract with NASA, and support by the Kepler Participating Scientist Program. S.B. acknowledges support from NSF grant AST-



1105930 and NASA grant NNX13AE70G. S.H. acknowledges financial support from the Netherlands organisation for Scientific Research and ERC starting grant #338251 (Stellar Ages). S.M. acknowledges support from the NASA grant NNX12AE17G. F.A.B. acknowledges support from a NASA Harriet Jenkins Fellowship and a Vanderbilt Provost Graduate Fellowship. W.J.C. acknowledges support from the UK Science and Technology Facilities Council (STFC). A.M.S. is supported by the MICINN grant AYA2011-24704 and by the ESF EUROCORES Program EuroGENESIS (MICINN grant EUI2009-04170). Funding for the Stellar Astrophysics Centre is provided by The Danish National Research Foundation (Grant agreement no.: DNR106). The re-

search is supported by the ASTERISK project (ASTERoseismic Investigations with SONG and Kepler) funded by the European Research Council (Grant agreement no.: 267864). This publication makes use of data products from the Two Micron All Sky Survey, which is a joint project of the University of Massachusetts and the Infrared Processing and Analysis Center/California Institute of Technology, funded by the National Aeronautics and Space Administration and the National Science Foundation. This research has made use of the NASA Exoplanet Archive, which is operated by the California Institute of Technology, under contract with the National Aeronautics and Space Administration under the Exoplanet Exploration Program.

## REFERENCES

- Allard, F., Homeier, D., & Freytag, B. 2012, Royal Society of London Philosophical Transactions Series A, 370, 2765
- Bakos, G. Á., et al. 2010, ApJ, 710, 1724
- Ballard, S., et al. 2011, ApJ, 743, 200
- , 2013, ApJ, 773, 98
- Bányai, E., et al. 2013, MNRAS, 436, 1576
- Baraffe, I., Chabrier, G., Allard, F., & Hauschildt, P. H. 1998, A&A, 337, 403
- Barclay, T., et al. 2012, ApJ, 761, 53
- , 2013a, Nature, 494, 452
- , 2013b, ApJ, 768, 101
- Bastien, F. A., Stassun, K. G., Basri, G., & Pepper, J. 2013, Nature, 500, 427
- Batalha, N. M., et al. 2010, ApJ, 713, L109
- , 2011, ApJ, 729, 27
- , 2013, ApJS, 204, 24
- Beck, P. G., et al. 2011, Science, 332, 205
- Bedding, T. R. 2011, ArXiv e-prints (arXiv:1107.1723)
- Bedding, T. R., et al. 2010, ApJ, 713, L176
- , 2011, Nature, 471, 608
- Belkacem, K., Goupil, M. J., Dupret, M. A., Samadi, R., Baudin, F., Noels, A., & Mosser, B. 2011, A&A, 530, A142
- Bonomo, A. S., et al. 2012, A&A, 538, A96
- Borucki, W. J., et al. 2010, Science, 327, 977
- , 2011a, ApJ, 728, 117
- , 2011b, ApJ, 736, 19
- , 2012, ApJ, 745, 120
- , 2013, Science, 340, 587
- Bouchy, F., et al. 2011, A&A, 533, A83
- Boyajian, T. S., et al. 2012, ApJ, 757, 112
- , 2013, ApJ, 771, 40
- Brown, T. M. 2010, ApJ, 709, 535
- Brown, T. M., Gilliland, R. L., Noyes, R. W., & Ramsey, L. W. 1991, ApJ, 368, 599
- Brown, T. M., Latham, D. W., Everett, M. E., & Esquerdo, G. A. 2011, AJ, 142, 112
- Bruntt, H., Frandsen, S., & Thygesen, A. O. 2011, A&A, 528, A121
- Bruntt, H., et al. 2010, MNRAS, 405, 1907
- , 2012, MNRAS, 423, 122
- Buchhave, L. A., et al. 2012, Nature, 486, 375
- Burke, C. J., et al. 2014, ApJS, 210, 19
- Cardelli, J. A., Clayton, G. C., & Mathis, J. S. 1989, ApJ, 345, 245
- Carter, J. A., et al. 2011, Science, 331, 562
- , 2012, Science, 337, 556
- Casagrande, L., Ramírez, I., Meléndez, J., Bessell, M., & Asplund, M. 2010, A&A, 512, A54
- Casagrande, L., Schönrich, R., Asplund, M., Cassisi, S., Ramírez, I., Meléndez, J., Bensby, T., & Feltzing, S. 2011, A&A, 530, A138
- Castelli, F., & Kurucz, R. L. 2004, ArXiv e-prints (arXiv:0405087)
- Catanzarite, J., & Shao, M. 2011, ApJ, 738, 151
- Chaplin, W. J., et al. 2011, Science, 332, 213
- , 2013, ApJ, 766, 101
- , 2014, ApJS, 210, 1
- Charpinet, S., et al. 2011, Nature, 480, 496
- Christensen-Dalsgaard, J., et al. 2010, ApJ, 713, L164
- Cochran, W. D., et al. 2011, ApJS, 197, 7
- Creevey, O. L., et al. 2013, MNRAS, 431, 2419
- Debosscher, J., Blomme, J., Aerts, C., & De Ridder, J. 2011, A&A, 529, A89
- Deheuvels, S., et al. 2012, ApJ, 756, 19
- Derekas, A., et al. 2011, Science, 332, 216
- Désert, J.-M., et al. 2011, ApJS, 197, 14
- Dong, S., Zheng, Z., & Zhu, Z. 2013, ArXiv e-prints (arXiv:1311.1203)
- Dong, S., & Zhu, Z. 2013, ApJ, 778, 53
- Dotter, A., Chaboyer, B., Jevremović, D., Kostov, V., Baron, E., & Ferguson, J. W. 2008, ApJS, 178, 89
- Doyle, L. R., et al. 2011, Science, 333, 1602
- Dressing, C. D., & Charbonneau, D. 2013, ApJ, 767, 95
- Dunham, E. W., et al. 2010, ApJ, 713, L136
- Eisenstein, D. J., et al. 2011, AJ, 142, 72
- Endl, M., et al. 2011, ApJS, 197, 13
- Everett, M. E., Howell, S. B., & Kinemuchi, K. 2012, PASP, 124, 316
- Everett, M. E., Howell, S. B., Silva, D. R., & Szkody, P. 2013, ApJ, 771, 107
- Fabrycky, D. C., et al. 2012, ApJ, 750, 114
- Faigler, S., Tal-Or, L., Mazeh, T., Latham, D. W., & Buchhave, L. A. 2013, ApJ, 771, 26
- Farmer, R., Kolb, U., & Norton, A. J. 2013, MNRAS, 433, 1133
- Fortney, J. J., et al. 2011, ApJS, 197, 9
- Frasca, A., Alcalá, J. M., Covino, E., Catalano, S., Marilli, E., & Paladino, R. 2003, A&A, 405, 149
- Fressin, F., et al. 2012, Nature, 482, 195
- , 2013, ApJ, 766, 81
- Gaidos, E. 2013, ApJ, 770, 90
- Gaidos, E., & Mann, A. W. 2013, ApJ, 762, 41
- García, R. A., et al. 2011, MNRAS, 414, L6
- Gilliland, R. L., et al. 2013, ApJ, 766, 40
- Girardi, L., Bressan, A., Bertelli, G., & Chiosi, C. 2000, A&AS, 141, 371
- González-Solares, E. A., et al. 2011, MNRAS, 416, 927
- Greiss, S., et al. 2012, AJ, 144, 24
- Grigahcène, A., et al. 2010, ApJ, 713, L192
- Hauschildt, P. H., Allard, F., & Baron, E. 1999, ApJ, 512, 377
- Hébrard, G., et al. 2013, A&A, 554, A114
- Hekker, S., Elsworth, Y., Mosser, B., Kallinger, T., Basu, S., Chaplin, W. J., & Stello, D. 2013, A&A, 556, A59
- Hekker, S., et al. 2010, MNRAS, 402, 2049
- , 2011, MNRAS, 414, 2594
- Holman, M. J., et al. 2010, Science, 330, 51
- Howard, A. W., et al. 2012, ApJS, 201, 15
- Howell, S. B., et al. 2010, ApJ, 725, 1633
- , 2012, ApJ, 746, 123
- Huber, D., Stello, D., Bedding, T. R., Chaplin, W. J., Arentoft, T., Quirion, P.-O., & Kjeldsen, H. 2009, Communications in Asteroseismology, 160, 74
- Huber, D., et al. 2011, ApJ, 731, 94
- , 2012, ApJ, 760, 32
- , 2013a, ApJ, 767, 127
- , 2013b, Science, 342, 331

- Jenkins, J. M., et al. 2010a, *ApJ*, 724, 1108  
— 2010b, *ApJ*, 713, L87
- Johnson, J. A., et al. 2012, *AJ*, 143, 111
- Jontof-Hutter, D., Lissauer, J. J., Rowe, J. F., & Fabrycky, D. C. 2013, ArXiv e-prints
- Jørgensen, B. R., & Lindegren, L. 2005, *A&A*, 436, 127
- Kallinger, T., et al. 2010, *A&A*, 522, A1
- Kawaler, S. D., et al. 2010, *MNRAS*, 409, 1487
- Koch, D. G., et al. 2010a, *ApJ*, 713, L131  
— 2010b, *ApJ*, 713, L79
- Kolenberg, K., et al. 2010, *ApJ*, 713, L198
- Kraus, A. L., Tucker, R. A., Thompson, M. I., Craine, E. R., & Hillenbrand, L. A. 2011, *ApJ*, 728, 48
- Kurtz, D. W., et al. 2011, *MNRAS*, 414, 2550
- Lissauer, J. J., et al. 2011, *Nature*, 470, 53  
— 2012, *ApJ*, 750, 112  
— 2013, *ApJ*, 770, 131
- Mann, A. W., Gaidos, E., Kraus, A., & Hilton, E. J. 2013, *ApJ*, 770, 43
- Mann, A. W., Gaidos, E., Lépine, S., & Hilton, E. J. 2012, *ApJ*, 753, 90
- Martín, E. L., Cabrera, J., Martioli, E., Solano, E., & Tata, R. 2013, *A&A*, 555, A108
- Mathur, S., et al. 2010, *A&A*, 518, A53  
— 2011, *ApJ*, 741, 119  
— 2012, *ApJ*, 749, 152
- Matijević, G., Prša, A., Orosz, J. A., Welsh, W. F., Bloemen, S., & Barclay, T. 2012, *AJ*, 143, 123
- Meibom, S., et al. 2013, *Nature*, 499, 55
- Mészáros, S., et al. 2013, *AJ*, 146, 133
- Miglio, A., et al. 2012, *MNRAS*, 419, 2077
- Molenda-Žakowicz, J., et al. 2013, *MNRAS*, 434, 1422
- Morel, T., & Miglio, A. 2012, *MNRAS*, 419, L34
- Morton, T. D., & Swift, J. J. 2013, ArXiv e-prints (arXiv:1303.3013)
- Mosser, B., & Appourchaux, T. 2009, *A&A*, 508, 877
- Mosser, B., et al. 2012a, *A&A*, 537, A30  
— 2012b, *A&A*, 548, A10  
— 2013, *A&A*, 559, A137
- Muirhead, P. S., Hamren, K., Schlawin, E., Rojas-Ayala, B., Covey, K. R., & Lloyd, J. P. 2012a, *ApJ*, 750, L37
- Muirhead, P. S., et al. 2012b, *ApJ*, 747, 144
- Nemec, J. M., Cohen, J. G., Ripepi, V., Derekas, A., Moskalik, P., Sesar, B., Chadid, M., & Bruntt, H. 2013, *ApJ*, 773, 181
- Nesvorný, D., Kipping, D. M., Buchhave, L. A., Bakos, G. Á., Hartman, J., & Schmitt, A. R. 2012, *Science*, 336, 1133
- Nordström, B., et al. 2004, *A&A*, 418, 989
- Nutzman, P., et al. 2011, *ApJ*, 726, 3
- Orosz, J. A., et al. 2012a, *Science*, 337, 1511  
— 2012b, *ApJ*, 758, 87
- Østensen, R. H., Bloemen, S., Vučković, M., Aerts, C., Oreiro, R., Kinemuchi, K., Still, M., & Koester, D. 2011, *ApJ*, 736, L39
- Petigura, E. A., Marcy, G. W., & Howard, A. W. 2013a, *ApJ*, 770, 69
- Petigura, E. A., Howard, A. W., & Marcy, G. W. 2013b, *PNAS*, 110, 19175
- Pietrinferni, A., Cassisi, S., Salaris, M., & Castelli, F. 2004, *ApJ*, 612, 168
- Pinsonneault, M., et al. 2014, in preparation
- Pinsonneault, M. H., An, D., Molenda-Žakowicz, J., Chaplin, W. J., Metcalfe, T. S., & Bruntt, H. 2012, *ApJS*, 199, 30
- Pont, F., & Eyer, L. 2004, *MNRAS*, 351, 487
- Prša, A., et al. 2011, *AJ*, 141, 83
- Rowe, J. F., et al. 2014, in preparation
- Sanchis-Ojeda, R., et al. 2013, *ApJ*, 775, 54
- Santerne, A., Bonomo, A. S., Hébrard, G., Deleuil, M., Moutou, C., Almenara, J.-M., Bouchy, F., & Díaz, R. F. 2011a, *A&A*, 536, A70
- Santerne, A., et al. 2011b, *A&A*, 528, A63
- Savitzky, A., & Golay, M. J. E. 1964, *Analytical Chemistry*, 36, 1627
- Seager, S., & Mallén-Ornelas, G. 2003, *ApJ*, 585, 1038
- Serenelli, A. M., Bergemann, M., Ruchti, G., & Casagrande, L. 2013, *MNRAS*, 429, 3645
- Silva Aguirre, V., et al. 2011, *ApJ*, 740, L2  
— 2012, *ApJ*, 757, 99
- Skrutskie, M. F., et al. 2006, *AJ*, 131, 1163
- Slawson, R. W., et al. 2011, *AJ*, 142, 160
- Smith, J. C., et al. 2012, *PASP*, 124, 1000
- Steffen, J. H., et al. 2012, *MNRAS*, 421, 2342
- Stello, D., Bruntt, H., Preston, H., & Buzasi, D. 2008, *ApJ*, 674, L53
- Stello, D., et al. 2013, *ApJ*, 765, L41
- Stumpe, M. C., et al. 2012, *PASP*, 124, 985
- Tenenbaum, P., et al. 2013, *ApJS*, 206, 5  
— 2014, *ApJS*, in press (arXiv:1311.0248)
- Thompson, S. E., et al. 2012, *ApJ*, 753, 86
- Thygesen, A. O., et al. 2012, *A&A*, 543, A160
- Torres, G., Andersen, J., & Giménez, A. 2010, *A&A Rev.*, 18, 67
- Torres, G., Fischer, D. A., Sozzetti, A., Buchhave, L. A., Winn, J. N., Holman, M. J., & Carter, J. A. 2012, *ApJ*, 757, 161
- Traub, W. A. 2012, *ApJ*, 745, 20
- Uytterhoeven, K., et al. 2011, *A&A*, 534, A125
- Valenti, J. A., & Fischer, D. A. 2005, *ApJS*, 159, 141
- Valenti, J. A., & Piskunov, N. 1996, *A&AS*, 118, 595
- van Leeuwen, F. 2007, *A&A*, 474, 653
- Verner, G. A., et al. 2011, *MNRAS*, 415, 3539
- Welsh, W. F., et al. 2012, *Nature*, 481, 475
- White, T. R., et al. 2013, *MNRAS*, 433, 1262
- Winn, J. N. 2010, ArXiv e-prints (arXiv:1001.2010)
- Wright, E. L., et al. 2010, *AJ*, 140, 1868
- Yanny, B., et al. 2009, *AJ*, 137, 4377
- Yi, S., Demarque, P., Kim, Y.-C., Lee, Y.-W., Ree, C. H., Lejeune, T., & Barnes, S. 2001, *ApJS*, 136, 417
- Zasowski, G., et al. 2013, *AJ*, 146, 81

TABLE 3  
REFERENCE KEY

Key	Reference	Methods
0	Brown et al. (2011)	Photometry
1	Pinsonneault et al. (2012)	Photometry
2	Dressing & Charbonneau (2013)	Photometry
3	Buchhave et al. (2012)	Spectroscopy
4	Uytterhoeven et al. (2011)	Spectroscopy
5	Muirhead et al. (2012a)	Spectroscopy
6	Bruntt et al. (2012)	Spectroscopy/Asteroseismology
7	Thygesen et al. (2012)	Spectroscopy/Asteroseismology
8	Huber et al. (2013a) <sup>+</sup>	Spectroscopy/Asteroseismology
9	Stello et al. (2013)	Asteroseismology
10	Chaplin et al. (2014)	Asteroseismology
11	Huber et al. (2011)	Asteroseismology
12	Petigura et al. (2013a)	Spectroscopy
13	Molenda-Żakowicz et al. (2013)	Spectroscopy
14	Mann et al. (2012)	Spectroscopy
15	Mann et al. (2013)	Spectroscopy
16	Gaidos (2013)	Photometry
17	Martín et al. (2013)	Spectroscopy
18	Batalha et al. (2013)	Spectroscopy/Transits
19	White et al. (2013)	Spectroscopy/Asteroseismology
20	Bakos et al. (2010)	Spectroscopy/Transits/EBs
21	Koch et al. (2010a)	Spectroscopy/Transits/EBs
22	Dunham et al. (2010)	Spectroscopy/Transits/EBs
23	Jenkins et al. (2010a)	Spectroscopy/Transits/EBs
24	Holman et al. (2010)	Spectroscopy/Transits/EBs
25	Lissauer et al. (2013)	Spectroscopy/Transits/EBs
26	Fortney et al. (2011)	Spectroscopy/Transits/EBs
27	Endl et al. (2011)	Spectroscopy/Transits/EBs
28	Doyle et al. (2011)	Spectroscopy/Transits/EBs
29	Désert et al. (2011)	Spectroscopy/Transits/EBs
30	Cochran et al. (2011)	Spectroscopy/Transits/EBs
31	Ballard et al. (2011)	Spectroscopy/Transits/EBs
32	Fressin et al. (2012)	Spectroscopy/Transits/EBs
33	Steffen et al. (2012)	Spectroscopy/Transits/EBs
34	Fabrycky et al. (2012)	Spectroscopy/Transits/EBs
35	Lissauer et al. (2012)	Spectroscopy/Transits/EBs
36	Welsh et al. (2012)	Spectroscopy/Transits/EBs
37	Orosz et al. (2012a)	Spectroscopy/Transits/EBs
38	Bouchy et al. (2011)	Spectroscopy/Transits/EBs
39	Santerne et al. (2011b)	Spectroscopy/Transits/EBs
40	Santerne et al. (2011a)	Spectroscopy/Transits/EBs
41	Muirhead et al. (2012b)	Spectroscopy/Transits/EBs
42	Bonomo et al. (2012)	Spectroscopy/Transits/EBs
43	Johnson et al. (2012)	Spectroscopy/Transits/EBs
44	Nesvorný et al. (2012)	Spectroscopy/Transits/EBs
45	Orosz et al. (2012b)	Spectroscopy/Transits/EBs
46	Ballard et al. (2013)	Spectroscopy/Transits/EBs
47	Meibom et al. (2013)	Spectroscopy/Transits/EBs
48	Barclay et al. (2013b)	Spectroscopy/Transits/EBs
49	Charpinet et al. (2011)	Spectroscopy/Transits/EBs
50	Howell et al. (2010)	Spectroscopy/Transits/EBs
51	Hébrard et al. (2013)	Spectroscopy/Transits/EBs
52	Faigler et al. (2013)	Spectroscopy/Transits/EBs
53	Sanchis-Ojeda et al. (2013)	Spectroscopy/Transits/EBs
54	This work	Photometry/Asteroseismology

<sup>+</sup> Includes references to the following published seismic solutions: Barclay et al. (2012); Christensen-Dalsgaard et al. (2010); Batalha et al. (2011); Chaplin et al. (2013); Borucki et al. (2012); Barclay et al. (2013a); Gilliland et al. (2013); Carter et al. (2012); Howell et al. (2012); Huber et al. (2013b).

TABLE 4  
 CONSOLIDATED INPUT VALUES

KIC	$T_{\text{eff}}$	$\log g$	[Fe/H]	$P_{T_{\text{eff}}}$	$P_{\log g}$	$P_{[\text{Fe}/\text{H}]}$
757076	5164 ± 154	3.601 ± 0.400	-0.083 ± 0.300	PHO1	KIC0	KIC0
757099	5521 ± 168	3.817 ± 0.400	-0.208 ± 0.300	PHO1	KIC0	KIC0
757137	4751 ± 139	2.378 ± 0.030	-0.079 ± 0.300	PHO1	AST9	KIC0
757280	6543 ± 188	4.082 ± 0.400	-0.231 ± 0.300	PHO1	KIC0	KIC0
757450	5330 ± 106	4.500 ± 0.050	-0.070 ± 0.150	SPE51	TRA51	SPE51
891901	6325 ± 186	4.411 ± 0.400	-0.084 ± 0.300	PHO1	KIC0	KIC0
891916	5602 ± 165	4.591 ± 0.400	-0.580 ± 0.300	PHO1	KIC0	KIC0
892010	4834 ± 151	2.163 ± 0.030	0.207 ± 0.300	PHO1	AST9	KIC0
892107	5086 ± 161	3.355 ± 0.400	-0.085 ± 0.300	PHO1	KIC0	KIC0
892195	5521 ± 184	3.972 ± 0.400	-0.054 ± 0.300	PHO1	KIC0	KIC0
...	...	...	...	...	...	...
1429653	6636 ± 225	4.622 ± 0.400	0.239 ± 0.300	PHO1	KIC0	KIC0
1429729	3903 ± 136	4.735 ± 0.400	-0.200 ± 0.300	PHO2	PHO2	PHO2
1429751	6000 ± 185	4.420 ± 0.400	-0.012 ± 0.300	PHO1	KIC0	KIC0
1429795	5772 ± 164	4.504 ± 0.400	-0.104 ± 0.300	PHO1	KIC0	KIC0
1429893	5068 ± 143	4.583 ± 0.400	-0.071 ± 0.300	PHO1	KIC0	KIC0
1429921	4356 ± 125	4.723 ± 0.400	-0.254 ± 0.300	PHO1	KIC0	KIC0
1429977	5155 ± 180	4.333 ± 0.400	-0.465 ± 0.300	KIC0	KIC0	KIC0
1430118	5070 ± 155	3.124 ± 0.030	-0.137 ± 0.300	PHO1	AST9	KIC0
1430163	6520 ± 130	4.221 ± 0.030	-0.110 ± 0.150	SPE6	AST10	SPE6
1430171	4771 ± 166	4.559 ± 0.400	-0.063 ± 0.300	KIC0	KIC0	KIC0
...	...	...	...	...	...	...

Note that all uncertainties were assigned typical fractional or absolute values for a given method, as listed in Table 2. Provenance abbreviations: KIC = Kepler Input Catalog, PHO = Photometry, SPE = Spectroscopy, AST = Asteroseismology, TRA = Transits. The number at the end of each provenance denotes the reference key, as given in Table 3. (This table is available in its entirety in a machine-readable form in the online journal. A portion is shown here for guidance regarding its form and content.)

 TABLE 5  
 Q1-Q16 STAR PROPERTIES CATALOG

KIC	Stellar Properties						Provenances			
	$T_{\text{eff}}$	$\log g$	[Fe/H]	$R(R_{\odot})$	$M(M_{\odot})$	$\rho$ (g cm <sup>-3</sup> )	$P_{T_{\text{eff}}}$	$P_{\log g}$	$P_{[\text{Fe}/\text{H}]}$	$P_{M,R,\rho}$
757076	5160 <sup>+138</sup> <sub>-163</sub>	3.580 <sup>+0.274</sup> <sub>-0.294</sub>	-0.100 <sup>+0.260</sup> <sub>-0.300</sub>	3.13 <sup>+1.41</sup> <sub>-1.03</sub>	1.36 <sup>+0.32</sup> <sub>-0.40</sub>	0.062 <sup>+0.112</sup> <sub>-0.040</sub>	PHO1	KIC0	KIC0	DSEP
757099	5519 <sup>+183</sup> <sub>-168</sub>	3.822 <sup>+0.501</sup> <sub>-0.276</sub>	-0.220 <sup>+0.340</sup> <sub>-0.280</sub>	2.11 <sup>+1.10</sup> <sub>-1.02</sub>	1.08 <sup>+0.33</sup> <sub>-0.20</sub>	0.16 <sup>+0.83</sup> <sub>-0.11</sub>	PHO1	KIC0	KIC0	DSEP
757137	4706 <sup>+81</sup> <sub>-103</sub>	2.374 <sup>+0.029</sup> <sub>-0.027</sub>	-0.100 <sup>+0.280</sup> <sub>-0.340</sub>	15.45 <sup>+3.57</sup> <sub>-4.60</sub>	2.06 <sup>+1.15</sup> <sub>-1.05</sub>	0.00079 <sup>+0.00035</sup> <sub>-0.00014</sub>	PHO1	AST9	KIC0	DSEP
757280	6543 <sup>+155</sup> <sub>-206</sub>	4.082 <sup>+0.228</sup> <sub>-0.266</sub>	-0.240 <sup>+0.240</sup> <sub>-0.300</sub>	1.64 <sup>+0.82</sup> <sub>-0.46</sub>	1.18 <sup>+0.30</sup> <sub>-0.17</sub>	0.38 <sup>+0.50</sup> <sub>-0.24</sub>	PHO1	KIC0	KIC0	DSEP
757450	5332 <sup>+102</sup> <sub>-98</sub>	4.500 <sup>+0.043</sup> <sub>-0.040</sub>	-0.080 <sup>+0.160</sup> <sub>-0.120</sub>	0.843 <sup>+0.051</sup> <sub>-0.044</sub>	0.821 <sup>+0.060</sup> <sub>-0.040</sub>	1.93 <sup>+0.30</sup> <sub>-0.26</sub>	SPE51	TRA51	SPE51	DSEP
891901	6324 <sup>+153</sup> <sub>-211</sub>	4.356 <sup>+0.085</sup> <sub>-0.327</sub>	-0.100 <sup>+0.300</sup> <sub>-0.300</sub>	1.15 <sup>+0.67</sup> <sub>-0.14</sub>	1.08 <sup>+0.11</sup> <sub>-0.11</sub>	1.01 <sup>+0.39</sup> <sub>-0.71</sub>	PHO1	KIC0	KIC0	DSEP
891916	5602 <sup>+183</sup> <sub>-148</sub>	4.587 <sup>+0.039</sup> <sub>-0.218</sub>	-0.580 <sup>+0.360</sup> <sub>-0.280</sub>	0.741 <sup>+0.286</sup> <sub>-0.056</sub>	0.773 <sup>+0.109</sup> <sub>-0.061</sub>	2.68 <sup>+0.48</sup> <sub>-1.50</sub>	PHO1	KIC0	KIC0	DSEP
892010	4729 <sup>+70</sup> <sub>-182</sub>	2.168 <sup>+0.032</sup> <sub>-0.027</sub>	0.070 <sup>+0.140</sup> <sub>-0.470</sub>	26.09 <sup>+0.44</sup> <sub>-1.47</sub>	3.652 <sup>+0.018</sup> <sub>-2.031</sub>	0.000290 <sup>+0.000158</sup> <sub>-0.000018</sub>	PHO1	AST9	KIC0	DSEP
892107	5080 <sup>+114</sup> <sub>-155</sub>	3.354 <sup>+0.261</sup> <sub>-0.299</sub>	-0.080 <sup>+0.220</sup> <sub>-0.320</sub>	4.29 <sup>+2.02</sup> <sub>-1.47</sub>	1.52 <sup>+0.37</sup> <sub>-0.32</sub>	0.027 <sup>+0.047</sup> <sub>-0.018</sub>	PHO1	KIC0	KIC0	DSEP
892195	5522 <sup>+190</sup> <sub>-157</sub>	3.984 <sup>+0.399</sup> <sub>-0.294</sub>	-0.060 <sup>+0.280</sup> <sub>-0.260</sub>	1.67 <sup>+0.97</sup> <sub>-0.65</sub>	0.98 <sup>+0.25</sup> <sub>-0.10</sub>	0.30 <sup>+0.93</sup> <sub>-0.20</sub>	PHO1	KIC0	KIC0	DSEP
...	...	...	...	...	...	...	...	...	...	...
1429653	6622 <sup>+174</sup> <sub>-314</sub>	4.331 <sup>+0.069</sup> <sub>-0.342</sub>	0.210 <sup>+0.150</sup> <sub>-0.430</sub>	1.32 <sup>+0.76</sup> <sub>-0.21</sub>	1.37 <sup>+0.22</sup> <sub>-0.28</sub>	0.83 <sup>+0.32</sup> <sub>-0.59</sub>	PHO1	KIC0	KIC0	DSEP
1429729	3903 <sup>+76</sup> <sub>-60</sub>	4.735 <sup>+0.060</sup> <sub>-0.070</sub>	-0.200 <sup>+0.200</sup> <sub>-0.100</sub>	0.523 <sup>+0.070</sup> <sub>-0.050</sub>	0.541 <sup>+0.070</sup> <sub>-0.050</sub>	5.33 <sup>+2.25</sup> <sub>-2.25</sub>	PHO2	PHO2	PHO2	DSEP2
1429751	6000 <sup>+156</sup> <sub>-194</sub>	4.415 <sup>+0.070</sup> <sub>-0.287</sub>	-0.020 <sup>+0.220</sup> <sub>-0.300</sub>	1.05 <sup>+0.45</sup> <sub>-0.12</sub>	1.04 <sup>+0.20</sup> <sub>-0.12</sub>	1.27 <sup>+0.40</sup> <sub>-0.81</sub>	PHO1	KIC0	KIC0	DSEP
1429795	5768 <sup>+153</sup> <sub>-150</sub>	4.501 <sup>+0.045</sup> <sub>-0.288</sub>	-0.100 <sup>+0.260</sup> <sub>-0.280</sub>	0.906 <sup>+0.377</sup> <sub>-0.080</sub>	0.950 <sup>+0.110</sup> <sub>-0.098</sub>	1.80 <sup>+0.38</sup> <sub>-1.14</sub>	PHO1	KIC0	KIC0	DSEP
1429893	5066 <sup>+158</sup> <sub>-130</sub>	4.578 <sup>+0.035</sup> <sub>-0.090</sub>	-0.080 <sup>+0.320</sup> <sub>-0.260</sub>	0.754 <sup>+0.120</sup> <sub>-0.059</sub>	0.785 <sup>+0.097</sup> <sub>-0.071</sub>	2.58 <sup>+0.45</sup> <sub>-0.76</sub>	PHO1	KIC0	KIC0	DSEP
1429921	4358 <sup>+127</sup> <sub>-136</sub>	4.673 <sup>+0.042</sup> <sub>-0.051</sub>	-0.260 <sup>+0.320</sup> <sub>-0.320</sub>	0.606 <sup>+0.061</sup> <sub>-0.055</sub>	0.629 <sup>+0.056</sup> <sub>-0.063</sub>	3.98 <sup>+0.84</sup> <sub>-0.75</sub>	PHO1	KIC0	KIC0	DSEP
1429977	5166 <sup>+192</sup> <sub>-158</sub>	4.554 <sup>+0.071</sup> <sub>-0.848</sub>	-0.440 <sup>+0.340</sup> <sub>-0.260</sub>	0.728 <sup>+1.287</sup> <sub>-0.076</sub>	0.692 <sup>+0.185</sup> <sub>-0.047</sub>	2.52 <sup>+0.78</sup> <sub>-2.39</sub>	KIC0	KIC0	KIC0	DSEP
1430118	5094 <sup>+82</sup> <sub>-167</sub>	3.126 <sup>+0.029</sup> <sub>-0.030</sub>	-0.100 <sup>+0.180</sup> <sub>-0.340</sub>	6.25 <sup>+0.51</sup> <sub>-1.61</sub>	1.90 <sup>+0.26</sup> <sub>-0.85</sub>	0.0110 <sup>+0.0039</sup> <sub>-0.0012</sub>	PHO1	AST9	KIC0	DSEP
1430163	6520 <sup>+84</sup> <sub>-84</sub>	4.221 <sup>+0.013</sup> <sub>-0.014</sub>	-0.110 <sup>+0.090</sup> <sub>-0.090</sub>	1.480 <sup>+0.030</sup> <sub>-0.030</sub>	1.340 <sup>+0.060</sup> <sub>-0.060</sub>	0.577 <sup>+0.024</sup> <sub>-0.025</sub>	SPE6	AST10	SPE6	MULT10
1430171	4771 <sup>+185</sup> <sub>-155</sub>	4.566 <sup>+0.050</sup> <sub>-0.051</sub>	-0.060 <sup>+0.300</sup> <sub>-0.280</sub>	0.729 <sup>+0.073</sup> <sub>-0.067</sub>	0.714 <sup>+0.092</sup> <sub>-0.058</sub>	2.60 <sup>+0.60</sup> <sub>-0.46</sub>	KIC0	KIC0	KIC0	DSEP
...	...	...	...	...	...	...	...	...	...	...

Reported are for each parameter the best-fitting value and the lower and upper limit of the 68% interval closest to the best-fit. Uncertainties set to zero indicate that no uncertainty estimate is available. Provenance abbreviations: KIC = Kepler Input Catalog, PHO = Photometry, SPE = Spectroscopy, AST = Asteroseismology, TRA = Transits, DSEP = Based on Dartmouth models, MULT = Based on multiple models (including DSEP). The number at the end of each provenance denotes the reference key, as given in Table 3. (This table is available in its entirety in a machine-readable form in the online journal. A portion is shown here for guidance regarding its form and content. An interactive version of this table is available at the NASA Exoplanet Archive: <http://exoplanetarchive.ipac.caltech.edu/>.)